

Fast Equivariant Imaging: Acceleration for Unsupervised Learning via Augmented Lagrangian and Auxiliary PnP Denoisers

Guixian Xu

*School of Mathematics,
University of Birmingham*

GXX422@STUDENT.BHAM.AC.UK

Jinglai Li

*School of Mathematics,
University of Birmingham*

J.LI.10@BHAM.AC.UK

Junqi Tang

*School of Mathematics,
University of Birmingham*

J.TANG.2@BHAM.AC.UK

Abstract

In this work, we propose Fast Equivariant Imaging (FEI), a novel unsupervised learning framework to rapidly and efficiently train deep imaging networks without ground-truth data. From the perspective of reformulating the Equivariant Imaging based optimization problem via the method of Lagrange multipliers and utilizing plug-and-play denoisers, this novel unsupervised scheme shows superior efficiency and performance compared to the vanilla Equivariant Imaging paradigm. In particular, our FEI schemes achieve an order-of-magnitude (10x) acceleration over standard EI on training U-Net for X-ray CT reconstruction and image inpainting, with improved generalization performance. In addition, the proposed scheme enables efficient test-time adaptation of a pretrained model to individual samples to secure further performance improvements. Extensive experiments show that the proposed approach provides a noticeable efficiency and performance gain over existing unsupervised methods and model adaptation techniques.

1. Introduction

Inverse problems are ubiquitous in sensing and imaging, playing a critical role in diverse domains ranging from medical imaging modalities, such as computed tomography (CT) and magnetic resonance imaging (MRI) (Sidky et al., 2006; Zbontar et al., 2019), to low-level vision tasks such as super-resolution and image inpainting (Dong et al., 2015; Yu et al., 2019). Solving these problems amounts to reconstructing the latent ground truth (GT) from a limited set of observed measurements. In general, these problems are ill-posed, as physical constraints often restrict the measurement dimensionality to be significantly lower than that of the target signal. Consequently, addressing the solution ambiguity caused by this ill-posedness remains the primary challenge in imaging inverse problems.

Modern learning-based solvers have emerged as a powerful paradigm, typically trained in a supervised manner using large external datasets that contain paired GT images and measurements (Xin et al., 2016;

Zhang and Ghanem, 2018). However, in certain domains, such as medical imaging, it is often prohibitively expensive or even impossible to obtain sufficient GT data for supervised learning (Belthangady and Royer, 2019). Consequently, models trained on such limited data are susceptible to distribution bias, which can lead to poor generalization performance on unseen test samples.

Recently, there has been an increased interest in developing various methodologies to address potential biases and poor generalization due to limited training data. Approaches based on *self-supervised internal learning*, exemplified by Deep Image Prior (DIP) (Ulyanov et al., 2018), leverage the inherent inductive bias of network architectures. DIP exploits the observation that untrained CNNs converge to regular structures faster than to noise during optimization. Although this approach allows for the precise exploitation of instance-specific characteristics, it incurs high computational costs as it necessitates optimizing the network from scratch for each test sample. In contrast, *self-supervised external learning* addresses the absence of ground truth data by training a shared model on a dataset of measurements (Quan et al., 2022; Chen et al., 2021, 2022). However, these methods generally suffer from the same limitation as supervised learning: susceptibility to poor generalization when test samples deviate from the training distribution.

Another significant line of research encompasses *unsupervised meta-learning* and *test-time adaptation* (TTA). Meta-learning aims to train a model capable of rapid adaptation to new tasks with minimal data. However, the majority of meta-learning approaches are supervised (Chi et al., 2021; Park et al., 2020), relying on GT images to fine-tune pre-trained models. Wang et al. (2024) proposed a hybrid strategy that involves supervised meta-training and self-supervised meta-testing for medical imaging, utilizing an equivariant-based self-supervised loss. In contrast, purely unsupervised meta-learning for inverse imaging problems remains underexplored. A notable exception is Qin et al. (2023), who proposed an unsupervised meta-learning framework for medical imaging employing a SURE-based loss.

Parallel to meta-learning, TTA seeks to adjust a pre-trained model during inference to align it with the test data distribution, thereby mitigating performance degradation. Darestani et al. (2022) demonstrated promising results by enforcing a data consistency (DC) loss during both the training phase and TTA. Specifically, they employ a self-supervised approach where reconstructed results are re-sampled to ensure consistency with the input measurements. However, relying solely on DC loss for TTA is often insufficient to learn robust self-supervised features (Chen et al., 2021), frequently resulting in suboptimal or even degraded reconstruction quality. Although Zhao et al. (2024) integrated self-supervised loss into deep unfolding networks via a lightweight adaptive layer, the considerable depth of the unrolled architecture results in slow adaptation speeds and limited robustness against significant distribution shifts.

Equivariant Imaging (EI) unifies *self-supervised external learning* and *test-time adaptation* through a natural objective based on equivariance consistency (Wang et al., 2024; Chen et al., 2021). This objective enforces consistency between the reconstructed images and the transformations applied to the input. Using the inherent symmetries of the imaging process and the physical measurement operator, EI facilitates more stable and effective learning and adaptation. However, EI faces significant computational and optimization challenges. Training is notably slower because each iteration requires multiple model evaluations, resulting in high computational overhead. Furthermore, the equivariant loss is fully effective only when the estimator achieves a near-perfect reconstruction. Consequently, this supervision signal is weak during the early stages of training, often leading to slow convergence.

In this work, we introduce Fast Equivariant Imaging (FEI), an efficient unsupervised training and adaptation framework that makes EI practical for high-dimensional tasks. FEI is based on a variable-splitting reformulation of the original EI objective that converts the single computationally expensive training problem into a sequence of simpler subproblems. Specifically, FEI alternates between two stages: a **latent-reconstruction step** that refines an auxiliary estimate of the ground truth, and a **pseudo-supervision step**

that enforces equivariance on the network using the refined latent. From an optimization perspective, variable splitting yields an equivalent constrained formulation that can be solved using Lagrangian methods (Afonso et al., 2010). While standard variable splitting (Afonso et al., 2010) requires exact subproblem minimization, recent advances in inexact optimization (Devolder et al., 2014) demonstrate that inexact updates with bounded errors are sufficient for convergence. Hence, we introduce a task-decoupled splitting strategy: the latent-reconstruction step focuses on solving the inverse problem via measurement fidelity and image priors, while the equivariance constraint is enforced as a regularization on the network parameters during the pseudo-supervision step. This design avoids the computationally expensive evaluation of equivariance gradients w.r.t. the latent variable, leading to substantial reductions in runtime and memory. Although we focus only on accelerating EI in this work, the same algorithmic structure can be easily extended to more recent variants of EI such as Robust Equivariant Imaging (REI) (Chen et al., 2022), Multi-Operator Imaging (MOI) (Tachella et al., 2022), and our recently proposed Sketched Equivariant Imaging (SkEI) (Xu et al., 2024), which utilizes dimensionality reduction techniques for acceleration.

We summarize the specific technical contributions of this work as follows:

- We propose an efficient unsupervised training paradigm FEI which conceptually splits the original brute-force EI training into two alternating steps: a Latent-Reconstruction Step and a Pseudo-Supervision Step. We demonstrate numerically that such a splitting can massively accelerate the unsupervised training of deep imaging networks.
- Under the FEI splitting framework, we propose two novel optimization schemes tailored for efficiently implementing FEI, based on a new integration of adaptive gradient methods (such as Adam) with inexact Half-Quadratic Splitting and Linearized ADMM. We utilized the gradient history of the subproblems from previous HQS/ADMM iterations to update the network parameters to ensure the fastest possible convergence.
- Building upon FEI, we also propose the first unsupervised training scheme PnP-FEI which utilizes pretrained denoisers for further numerical improvements. Thanks to the splitting provided by FEI, we can effectively utilize pretrained image-domain priors such as deep denoiser within our framework, in the Latent-Reconstruction Step. This is the first paradigm which utilizes both the primal domain (image) prior and the dual domain (measurement) prior for unsupervised training of deep imaging networks.
- In addition, we demonstrate that the proposed scheme enables efficient test-time adaptation of a pre-trained model to individual samples to secure further performance improvements and robustness towards distribution shifts.

2. Related Work

Variable Splitting The variable splitting strategy, originally formalized by Afonso et al. (2010), decouples the data fidelity term from non-smooth regularization components. This strategy has been widely adopted to guide deep unrolling frameworks in supervised learning, such as Zhang et al. (2020); Chan et al. (2016); Yang et al. (2018). Beyond supervised learning, variable splitting has proven critical for stabilizing deep image prior (DIP), approaches like DeepRED (Mataev et al., 2019) utilize splitting to impose explicit regularization (e.g., RED) on the network output, effectively mitigating the overfitting and instability inherent

to original DIP optimization. Furthermore, this modularity extends to self-supervised learning, where architectures like DURED-Net (Huang et al., 2023) leverage variable splitting to isolate data consistency from denoising tasks, enabling robust physics-guided reconstruction via measurement splitting across multiple undersampled operators. To the best of our knowledge, this work is the first to extend variable splitting to the more challenging unsupervised setting involving single-operator inverse problems. This domain notably encompasses critical applications such as sparse-view CT and accelerated MRI with fixed sampling masks.

Equivariant Imaging Among unsupervised approaches for training deep imaging networks, the Equivariant Imaging (EI) framework (Chen et al., 2021, 2022) pioneered the explicit recovery of information beyond the range space of the physical operator by exploiting the inherent symmetries of imaging systems. EI posits that the distribution of clean images is invariant under specific geometric transformations, such as translations, rotations, and flips. Accordingly, it introduces a training loss that enforces equivariance throughout the measurement-reconstruction process, thereby constraining the set of learnable models. This unsupervised paradigm has recently achieved state-of-the-art performance in a diverse array of inverse problems (Wang and Davies, 2024; Terris et al., 2024). However, one of the main challenges of these schemes is the computational cost of training due to slow convergence and large computational complexity between training iterations, particularly for large-scale inverse problems and advanced architectures such as unrolling (Monga et al., 2021; Zhou et al., 2024). In our recent work of Sketched EI (Xu et al., 2024) we partially addressed the computational complexity issue for inverse problems on which dimensionality reduction strategies can be applied.

Test-Time Adaptation TTA adapts a pre-trained model during the inference phase without accessing the original source data. The primary objective is to align the model with the specific distribution of the test data, thus enhancing performance in the target domain. By operating in a source-free manner, TTA effectively addresses concerns regarding data privacy and availability. To compensate for the absence of ground truth (GT) supervision during adaptation, various self-supervised loss functions have been proposed. For instance, MetaCS (Qin et al., 2023) introduced a self-supervised loss based on Stein’s Unbiased Risk Estimator (SURE) for unsupervised meta-learning. Similarly, DDSSL (Quan et al., 2022) developed a self-supervised dual-domain loss specifically tailored for TTA in medical imaging contexts. However, while these approaches mitigate the reliance on GT images, their performance generally remains inferior to that of fully supervised methods.

3. Background

3.1 Problem setup

In this work, we address linear inverse imaging problems modeled as:

$$\mathbf{y} \approx \mathbf{A}\mathbf{x}^\dagger, \tag{1}$$

where $\mathbf{x}^\dagger \in \mathbb{R}^n$ denotes the unknown signal to be estimated and $\mathbf{y} \in \mathbb{R}^m$ represents the noisy measurements. The forward operator is given by $\mathbf{A} \in \mathbb{R}^{m \times n}$, often representing an ill-posed setting where $m \ll n$. In this context, a Maximum A Posteriori (MAP) estimator for \mathbf{x}^\dagger can be formulated as the solution to the following optimization problem:

$$\mathbf{x}^* = \arg \min_{\mathbf{x}} \{f_{\text{mc}}(\mathbf{A}\mathbf{x}, \mathbf{y}) + R(\mathbf{x})\}, \tag{2}$$

where $f_{\text{mc}}(\mathbf{A}\mathbf{x}, \mathbf{y})$ is the measurement consistency (MC) term such as ℓ_1 loss, ℓ_2 loss and SURE-loss (Chen et al., 2022), $R(\mathbf{x})$ is the prior or regularizer. Typically, learning based methods seek to train a network

$$\mathcal{F}_\theta(\mathbf{y}) \rightarrow \mathbf{x} \quad (3)$$

approximating the solution of the aforementioned optimization problem. The network \mathcal{F}_θ can be trained using supervised or unsupervised strategies. Our focus lies on the latter scenario, where training is based solely on measurement data without access to ground-truth images. This is achieved primarily by enforcing measurement consistency, often complemented by additional regularization or self-supervised objectives.

3.2 Equivariant Imaging

To enforce data fidelity, we formulate the Measurement Consistency (MC) objective as:

$$\min_{\theta} \mathbb{E}_{\mathbf{y} \in \mathcal{Y}} f_{\text{mc}}(\mathbf{A}\mathcal{F}_\theta(\mathbf{y}), \mathbf{y}). \quad (\text{MC})$$

However, relying solely on the MC constraint is insufficient to uniquely determine the inverse mapping. As noted in Chen et al. (2021), this objective does not recover signal components lying within the null space of the forward operator \mathbf{A} .

To recover information lost during the forward process, Chen et al. (2021) leverages prior information about the inherent symmetries of the signal set. Specifically, the distribution of plausible images is assumed to be invariant under certain groups of transformations (e.g., shifts, rotations). This symmetry implies that the composition $\mathcal{F}_\theta \circ \mathbf{A}$ should be equivariant to the transformation T_g :

$$\mathcal{F}_\theta(\mathbf{A}T_g\mathbf{x}^\dagger) = T_g\mathcal{F}_\theta(\mathbf{A}\mathbf{x}^\dagger) \quad (4)$$

where $T_g \in \mathbb{R}^{n \times n}$ denotes a unitary matrix representation of the group element \mathcal{G} . This equivariant regularization leads to the following unsupervised learning paradigm:

$$\min_{\theta} \mathbb{E}_{\mathbf{y} \in \mathcal{Y}, g \sim \mathcal{G}} \{f_{\text{mc}}(\mathbf{y}, \mathbf{A}\mathcal{F}_\theta(\mathbf{y})) + \alpha \|T_g\mathcal{F}_\theta(\mathbf{y}) - \mathcal{F}_\theta(\mathbf{A}T_g\mathcal{F}_\theta(\mathbf{y}))\|_2^2\}, \quad (5)$$

where $\alpha > 0$ is a trade-off coefficient. While EI has recently achieved state-of-the-art performance for various inverse problems (Chen et al., 2021, 2022; Terris et al., 2024), its effectiveness relies on the condition $T_g(\mathcal{F}_\theta \circ \mathbf{A})\mathbf{x}^\dagger \approx (\mathcal{F}_\theta \circ \mathbf{A})T_g\mathbf{x}^\dagger$. This relationship implies that the equivariant loss provides most meaningful gradients primarily when the estimator is already capable of near-perfect reconstruction ($\mathcal{F}_\theta(\mathbf{y}) \approx \mathbf{x}^\dagger$). However, this condition is rarely met during the early stages of training, resulting in an inefficient optimization trajectory.

3.3 Variable Splitting and Inexact Optimization

One strategy to address the limitations of EI is to employ variable splitting (Afonso et al., 2010). Variable splitting is a standard technique used to reformulate an unconstrained optimization problem of the form:

$$\min_{\mathbf{u} \in \mathbb{R}^n} f_1(\mathbf{u}) + f_2(g(\mathbf{u})) \quad (6)$$

where $g: \mathbb{R}^n \rightarrow \mathbb{R}^d$. We introduce an auxiliary variable $\mathbf{v} \in \mathbb{R}^d$ to decouple the argument of f_2 , imposing the constraint $g(\mathbf{u}) = \mathbf{v}$. This yields the equivalent constrained formulation:

$$\min_{\mathbf{u} \in \mathbb{R}^n, \mathbf{v} \in \mathbb{R}^d} f_1(\mathbf{u}) + f_2(\mathbf{v}), \quad \text{subject to } g(\mathbf{u}) = \mathbf{v}. \quad (7)$$

Problem (7) is equivalent to the unconstrained problem (6) over the feasible set $\{(\mathbf{u}, \mathbf{v}) : g(\mathbf{u}) = \mathbf{v}\}$. The key idea is that solving the decoupled constrained problem (7) is often computationally more tractable than solving its unconstrained counterpart (6), particularly when splitting allows for the use of efficient solvers for the sub-problems.

Standard splitting methods typically require the exact minimization of subproblems to guaranty convergence. However, in large-scale imaging tasks, exact solutions are often computationally intractable. Inexact splitting methods relax this requirement, allowing subproblems to be solved approximately (e.g., via limited gradient steps or by omitting complex regularization terms) while maintaining convergence under bounded error conditions (Devolder et al., 2014; Yang and Yuan, 2013; Robini et al., 2018, 2016). Our FEI framework builds on this theoretical foundation.

4. Method

In this section, we present our fast Equivariant Imaging (FEI) framework, which is based on splitting the original objective of EI into multiple subproblems. The original EI is enforced $T_g \mathcal{F}_\theta(\mathbf{y}) \approx \mathcal{F}_\theta(\mathbf{A} T_g \mathcal{F}_\theta(\mathbf{y}))$. Crucially, the underlying assumption $T_g(\mathcal{F}_\theta \circ \mathbf{A})\mathbf{x}^\dagger = (\mathcal{F}_\theta \circ \mathbf{A})T_g\mathbf{x}^\dagger$ holds strictly at the ground truth \mathbf{x}^\dagger . This implies that the equivariant loss is most effective when the estimator achieves near-perfect reconstruction, i.e., $\mathcal{F}_\theta(\mathbf{y}) \approx \mathbf{x}^\dagger$. Consequently, improving reconstruction quality facilitates the enforcement of equivariance (see Figure 1 for numerical verification). Based on this insight, we propose decomposing the original optimization problem into multiple steps: **Latent-reconstruction** and **Pseudo-supervision**.

Denote the Latent-reconstruction mapping as

$$M_L(\mathbf{y}, \mathcal{F}_{\theta_k}) \rightarrow \mathbf{u}_{k+1},$$

which takes current network output at a data sample \mathbf{y} and form a latent image \mathbf{u}_{k+1} . We then also denote the Pseudo-supervision mapping as

$$M_P(\mathbf{u}_{k+1}, \mathcal{F}_{\theta_k}) \rightarrow \theta_{k+1}$$

which takes the latent image to perform the update on network parameters joint-force with EI-regularization. Then we can describe our generic FEI framework here:

FEI generic framework

–Initialize θ_0

For $k = 0, 1, 2, \dots, K$

$$\left[\begin{array}{ll} \text{Sample } \mathbf{y} \in \mathcal{Y}, g \sim \mathcal{G} & \\ \mathbf{u}_{k+1} \leftarrow M_L(\mathbf{y}, \mathcal{F}_{\theta_k}) & \textit{Latent reconstruction} \\ \theta_{k+1} \leftarrow M_P(\mathbf{u}_{k+1}, \mathcal{F}_{\theta_k}) & \textit{Pseudo supervision} \end{array} \right.$$

This leads to (at least) two options for FEI algorithmically, one with a style of Half-Quadratic Splitting (HQS), and one with a style of Linearized ADMM. We build our numerical training algorithms for implementing FEI via modifying both HQS and ADMM splitting and tailoring them for unsupervised training of deep imaging networks. Crucially, addressing the equivariance constraint $\alpha \|T_g \mathbf{u} - \mathcal{F}_\theta(\mathbf{A} T_g \mathbf{u})\|^2$ strictly within the latent-reconstruction step (updating \mathbf{u}) poses a significant computational bottleneck. It would require backpropagation through the network \mathcal{F}_θ at every inner iteration of the solver, thus negating the efficiency gains of variable splitting. To avoid this, we propose a relaxed splitting scheme that decouples equivariance enforcement from latent variable update. We specifically assign the role of maintaining

equivariance to the network parameter update step (Pseudo-supervision), while the latent step focuses on enforcing measurement consistency and signal priors.

Mathematically, the inexactness of the proposed relaxed splitting scheme originates from a latent reconstruction step:

$$F(\mathbf{u}) = \underbrace{f_{\text{mc}}(\mathbf{y}, \mathbf{A}\mathbf{u}) + \frac{\lambda}{2} \|\mathbf{u} - \mathcal{F}_\theta(\mathbf{y})\|^2}_{\text{Proximal Objective } \Phi(\mathbf{u})} + \underbrace{\alpha \|\mathbb{T}_g \mathbf{u} - \mathcal{F}_\theta(\mathbf{A}\mathbb{T}_g \mathbf{u})\|^2}_{\text{Equivariance Term } \Psi(\mathbf{u})} \quad (8)$$

where the gradient term here is $\nabla F(\mathbf{u}) = \nabla \Phi(\mathbf{u}) + \nabla \Psi(\mathbf{u})$, while FEI proposes to solve the \mathbf{u} -subproblem with approximate gradient $g(\mathbf{u}) = \nabla \Phi(\mathbf{u})$, therefore, there is an error between the exact gradient $\nabla F(\mathbf{u})$ and the inexact gradient $g(\mathbf{u})$, which we denote as

$$e(\mathbf{u}) = \nabla F(\mathbf{u}) - g(\mathbf{u}) = \nabla \Psi(\mathbf{u}). \quad (9)$$

In order to theoretically show the convergence of this inexact approximation, we introduce the following mild assumptions.

Assumption 4.1 (L-Smoothness of the Objective) $F(\mathbf{u})$ is L is differentiable and its gradient $\nabla F(\mathbf{u})$ is Lipschitz continuous with constant $L > 0$, i.e.,

$$\|\nabla F(\mathbf{u}) - \nabla F(\mathbf{v})\| \leq L \|\mathbf{u} - \mathbf{v}\|, \quad \forall \mathbf{u}, \mathbf{v} \in \mathbb{R}^n. \quad (10)$$

Assumption 4.2 (Bounded Equivariance Gradient) We assume that the gradient of the equivariance regularization term, denoted as the error vector $e(\mathbf{u}) = \nabla \Psi(\mathbf{u})$, is uniformly bounded during the iterations. That is, there exists a constant $\delta_\infty \geq 0$ such that for all k :

$$\|e(\mathbf{u}_k)\| \leq \delta_k, \quad \text{and} \quad \limsup_{k \rightarrow \infty} \delta_k \leq \delta_\infty. \quad (11)$$

Furthermore, we assume the network architecture \mathcal{F}_θ has sufficient capacity to approximate the equivariant manifold, such that the equivariance error remains controlled.

Remark (Interpretation of Bounded Equivariance Gradient): The omission of the equivariance term in Eq. (8) renders the \mathbf{u} -update an inexact proximal step with respect to the full objective $F(\mathbf{u})$. Moreover, the omitted gradient term is θ -parameterized with the form

$$\nabla_{\mathbf{u}} \Psi(\mathbf{u}) = 2\alpha \mathbb{T}_g^T (\mathbb{T}_g \mathbf{u} - \mathcal{F}_\theta(\mathbf{A}\mathbb{T}_g \mathbf{u})) - 2\alpha \mathbb{T}_g^T \mathbf{A}^T \underbrace{J_{\mathcal{F}}(\mathbf{A}\mathbb{T}_g \mathbf{u})^T (\mathbb{T}_g \mathbf{u} - \mathcal{F}_\theta(\mathbf{A}\mathbb{T}_g \mathbf{u}))}_{\text{Jacobian}}, \quad (12)$$

as the network \mathcal{F}_θ becomes more equivariant (via the θ -step), the value of $(\mathbb{T}_g \mathbf{u} - \mathcal{F}_\theta(\mathbf{A}\mathbb{T}_g \mathbf{u}))$ decreases (as numerically verified in Figure 1), effectively reducing the inexactness gap δ_k as training progresses.

Now we are ready to show the main theoretical results.

Proposition 4.3 (Convergence of Inexact Latent Step) If FEI's iteration is performed using step size $\eta = 1/2L$ with $\mathbf{u}_{t+1} = \mathbf{u}_t - \eta g(\mathbf{u}_t)$, then the decrease in the objective function value $F(\mathbf{u})$ satisfies:

$$F(\mathbf{u}_{t+1}) \leq F(\mathbf{u}_t) - \frac{1}{8L} \|\nabla \Phi(\mathbf{u}_t)\|^2 + \frac{1}{4L} \delta_t^2, \quad (13)$$

this implies that provided δ_t is sufficiently small (or suppressed by the θ update step), the Latent Step guarantees that the objective function $F(\mathbf{u})$ will tend towards a decreasing trajectory, or at least oscillate within a neighborhood of radius δ without diverging.

Proof See Appendix. ■

Theorem 4.4 (Global Asymptotic Convergence to an Error Neighborhood) *Suppose Assumptions 4.1 and Assumption 4.2 hold. Let the step size be set to $\eta = \frac{1}{L}$. Then, the sequence $\{\mathbf{u}_k\}$ generated by the FEI latent reconstruction step satisfies:*

$$\liminf_{k \rightarrow \infty} \|\nabla F(\mathbf{u}_k)\|^2 \leq \delta_\infty^2.$$

This implies that the algorithm converges to an neighborhood of the critical point of $F(\mathbf{u})$, where the radius of the neighborhood is determined by the asymptotic magnitude of the equivariance gradient error δ_∞ .

Proof See Appendix. ■

Remark (Interpretation of the Error Bound) Theorem 4.4 establishes that the FEI algorithm does not necessarily converge to a stationary point ($\nabla F = 0$) in the classical sense, which is consistent with the inexact nature of the splitting. Instead, the algorithm is guaranteed to reach a state in which the gradient of the objective is bounded by the magnitude of the equivariance error δ_∞ . Ideally, if the network \mathcal{F}_θ learns to be perfectly equivariant, i.e., $\nabla \Psi(\mathbf{u}) \rightarrow 0$, then $\delta_\infty = 0$, and the standard global convergence to a critical point is recovered.

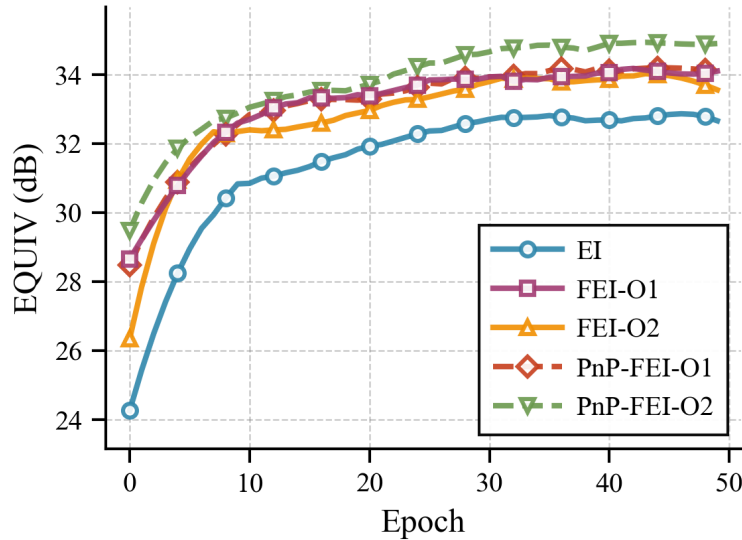


Figure 1: Evolution of the EQUIV metric (refer to Sec. 5) during the early stages of training. These results are derived from a proof-of-concept sparse-view CT experiment using a small-scale dataset comprising 10 training samples and 10 held-out test samples. Notably, this implies that FEI significantly facilitates the enforcement of equivariance constraints during the initial training phase.

Moreover, apart from those huge benefits in terms of computational efficiency and generalization performance, the flexibility resulting from the splitting structure of FEI allows us to build for the first time an ultimate method PnP-FEI which utilizes both **primal and dual priors** for further improved training of deep imaging network: while EI acts as a powerful dual (measurement) domain regularization, we can also introduce primal (image) domain priors (e.g. via plug-and-play denoisers) in the latent-reconstruction step.

4.1 Fast Equivariant Imaging — Option 1 (Inexact Half Quadratic Splitting)

We first reformulate (5) by substituting $\mathbf{u} = \mathcal{F}_\theta(\mathbf{y})$ as follows

$$\min_{\theta, \mathbf{u}} \mathbb{E}_{\mathbf{y} \in \mathcal{Y}, g \sim \mathcal{G}} \{f_{\text{mc}}(\mathbf{y}, \mathbf{A}\mathbf{u}) + \alpha \|\mathbf{T}_g \mathbf{u} - \mathcal{F}_\theta(\mathbf{A}\mathbf{T}_g \mathbf{u})\|_2^2\}, \quad \text{s.t. } \mathbf{u} = \mathcal{F}_\theta(\mathbf{y}). \quad (14)$$

To solve this constraint problem with the choice of Euclidean norm of f , we first rewrite the Lagrangian with penalty parameter λ ,

$$\mathcal{L}_{\lambda, \alpha}(\mathbf{u}, \theta) = \mathbb{E}_{\mathbf{y} \in \mathcal{Y}, g \sim \mathcal{G}} \{f_{\text{mc}}(\mathbf{y}, \mathbf{A}\mathbf{u}) + \frac{\lambda}{2} \|\mathbf{u} - \mathcal{F}_\theta(\mathbf{y})\|_2^2 + \alpha \|\mathbf{T}_g \mathbf{u} - \mathcal{F}_\theta(\mathbf{A}\mathbf{T}_g \mathbf{u})\|_2^2\}. \quad (15)$$

We then address problem (15) with half quadratic splitting (HQS) algorithm due to its simplicity. Note that a very large λ will force \mathbf{u} to be approximately equal to $\mathcal{F}_\theta(\mathbf{y})$. Usually, λ varies in a non-descending order during the following iterative solution

$$\mathbf{u}_{t+1} \approx \arg \min_{\mathbf{u}} \mathcal{L}_{\lambda, \alpha}(\mathbf{u}, \theta_t); \quad \rightarrow \textit{Latent reconstruction step} \quad (16)$$

$$\theta_{t+1} \approx \arg \min_{\theta} \mathcal{L}_{\lambda, \alpha}(\mathbf{u}_{t+1}, \theta); \quad \rightarrow \textit{Pseudo supervision step} \quad (17)$$

To ensure the convexity and computational tractability of the \mathbf{u} -update, we adopt an inexact Half-Quadratic Splitting (HQS) strategy where the equivariance regularization is deferred to the network update step (θ). Consequently, the latent reconstruction subproblem (16) simplifies to refine the estimate \mathbf{u} :

$$\min_{\mathbf{u}} \mathbb{E}_{\mathbf{y} \in \mathcal{Y}} \left\{ f_{\text{mc}}(\mathbf{A}\mathbf{u}, \mathbf{y}) + \frac{\lambda}{2} \|\mathbf{u} - \mathcal{F}_\theta(\mathbf{y})\|_2^2 \right\}. \quad (18)$$

We propose solving (18) via Nesterov Accelerated Gradient (NAG) (Nesterov, 1983, 2007). Of course, one could also use other optimizers, such as stochastic gradient methods (Ehrhardt et al., 2025) (if the objective can be minibatched) or quasi-Newton methods (Tan et al., 2024) for this step.

However, the Lagrangian with respect to θ is nonconvex, which means the minimization over θ is often intractable. Here we bypass it by calling backpropagating over θ and taking one gradient descent step using an adaptive gradient method (Adam by default). The complete algorithm for Lagrangian-based fast equivariant imaging can be found in Algorithm 1. Note that in each iteration we typically just run one iteration of Adam for the Pseudo-supervision step, while the gradient and momentum history of Adam is inherited from previous Pseudo-supervision steps.

4.2 Fast Equivariant Imaging — Option 2 (Linearized ADMM Splitting)

We now present the second option of splitting style for FEI, which is based on modifying the ADMM splitting and tailoring it to unsupervised learning for imaging. First, starting with (14), we turn the constraint into a penalty using the Augmented Lagrangian (AL) (Afonso et al., 2010),

$$\mathcal{L}_{\lambda, \alpha}(\mathbf{u}, \theta, \mathbf{L}) := \mathbb{E}_{\mathbf{y} \in \mathcal{Y}, g \in \mathcal{G}} \{f_{\text{mc}}(\mathbf{y}, \mathbf{A}\mathbf{u}) + \alpha \|\mathbf{T}_g \mathbf{u} - \mathcal{F}_\theta(\mathbf{A}\mathbf{T}_g \mathbf{u})\|_2^2 + \langle \mathbf{L}, \mathbf{u} - \mathcal{F}_\theta(\mathbf{y}) \rangle + \frac{\lambda}{2} \|\mathbf{u} - \mathcal{F}_\theta(\mathbf{y})\|_2^2\} \quad (19)$$

for a penalty weight $\lambda > 0$. Applied to (19), every iteration of ADMM would minimize the Augmented Lagrange with respect to \mathbf{u} , then with respect to θ , and then update the dual variable \mathbf{L} , which are presented as follows:

$$\begin{aligned} \mathbf{u}_{k+1} &\approx \arg \min_{\mathbf{u}} \mathcal{L}_{\lambda, \alpha}(\mathbf{u}, \theta_k, \mathbf{L}_k), \quad \rightarrow \textit{Latent reconstruction step} \\ \theta_{k+1} &\approx \arg \min_{\theta} \mathcal{L}_{\lambda, \alpha}(\mathbf{u}_{k+1}, \theta, \mathbf{L}_k), \quad \rightarrow \textit{Pseudo supervision step} \\ \mathbf{L}_{k+1} &= \mathbf{L}_k - (\mathbf{u}_{k+1} - \mathcal{F}_{\theta_{k+1}}(\mathbf{y})). \end{aligned} \quad (20)$$

Algorithm 1 Fast Equivariant Imaging (FEI-Option 1)

1: **Inputs:**

- \mathcal{Y} - Observations (training dataset)
- λ - Lagrangian multiplier
- α - EI regularization parameter
- N - number of epochs
- \mathbf{u}_0 - initial NAG point
- \mathbf{v}_0 - initial NAG velocity point
- β - NAG momentum factor
- η - NAG step size
- J - number of NAG iterations
- \mathcal{G} - Group of transformations

2: **Initialize:** Neural network \mathcal{F}_θ , $\mathbf{u}_0 = \mathbf{A}^\dagger \mathbf{y}$, $\mathbf{v}_0 = \mathbf{0}$, $k = 0$;3: **For** $i = 0, \dots, N - 1$ do:4: **For** $\mathbf{y} \in \mathcal{Y}$ do:5: Sample T_g where $g \sim \mathcal{G}$;6: Compute $\mathbf{x}_0 = \mathcal{F}_{\theta_k}(\mathbf{y})$, $\mathbf{u}_k = \mathbf{x}_0$;7: Set $f(\mathbf{u}) = f_{\text{mc}}(\mathbf{y}, \mathbf{A}\mathbf{u}) + \frac{\lambda}{2} \|\mathbf{u} - \mathcal{F}_{\theta_k}(\mathbf{y})\|_2^2$;8: Update $\mathbf{u}_{k+1} = \mathcal{A}(f, J, \mathbf{u}_k, \mathbf{v}_k, \beta, \eta)$ via NAG algorithm;9: Let $\mathbf{x}_1 = \mathbf{u}_{k+1}$;10: Transform $\mathbf{x}_2 = T_g(\mathbf{x}_1)$;11: Compute $\mathbf{x}_3 = \mathcal{F}_\theta(\mathbf{A}\mathbf{x}_2)$;12: Update θ_{k+1} via progressively minimizing loss $\mathcal{L} = \mathbb{E}_{g \sim \mathcal{G}} \{ \|\mathbf{x}_0 - \mathbf{x}_1\|_2^2 + \alpha \|\mathbf{x}_2 - \mathbf{x}_3\|_2^2 \}$ using a gradient-based optimizer (such as Adam) in each iteration;13: $k \leftarrow k + 1$ 14: **End For**15: **End For**16: **Output:** \mathcal{F}_{θ^*}

then take only one descent step in both \mathbf{u} and θ . Specifically, fixing θ_k, \mathbf{L}_k , the update of \mathbf{u}_{k+1} can be performed by one step gradient descent on the measurement consistency and Lagrangian terms. Consistent with our inexact splitting formulation, the equivariance regularization is reserved for the subsequent θ -update step to avoid nested gradient evaluations. Then fixing $\mathbf{u}_{k+1}, \mathbf{L}_k$, the update of θ is done by calling backpropagating and taking one adaptive gradient descent (Adam by default) step θ . Note that in each iteration we typically just run one iteration of Adam for the Pseudo-supervision step, while the gradient and momentum history of Adam is inherited from previous Pseudo-supervision steps. As for the Lagrange multiplier vector \mathbf{L} , its update is much easier, given by

$$\mathbf{L}_{k+1} = \mathbf{L}_k - (\mathbf{u}_{k+1} - \mathcal{F}_{\theta_{k+1}}(\mathbf{y})) \quad (21)$$

as emerging from the AL method (Afonso et al., 2010).

4.3 PnP-FEI: Utilizing Both Primal and Dual Priors

FEI provides us with a powerful way of effectively and efficiently utilizing the dual-domain prior such as EI for unsupervised training of deep imaging networks. Since in FEI we split the training problem with a latent-reconstruction, we can also choose to utilize the primal (image) domain prior to further accelerate the training and improve the performance. The plug-and-play (Venkatakrishnan et al., 2013) prior is a flexible framework that incorporates state-of-the-art denoising algorithms as priors in more challenging

Algorithm 2 Fast Equivariant Imaging (FEI-Option 2)

 1: **Inputs:**

- \mathcal{Y} - Observations (training dataset)
- \mathbf{L} - Augmented Lagrangian multiplier
- λ - Augmented Lagrangian free parameter
- α - EI regularization parameter
- N - number of epochs
- \mathcal{G} - Group of transformations
- \mathbf{u}_0 - Initial gradient descent point of (20)
- γ - Gradient descent step size

 2: **Initialize:** Neural network \mathcal{F}_θ , $\mathbf{L}_0 = \mathbf{0}$, $\mathbf{u}_0 = \mathbf{0}$, $k = 0$;

 3: **For** $i = 0, \dots, N - 1$ **do**:

 4: **For** $\mathbf{y} \in \mathcal{Y}$ **do**:

 5: Sample T_g where $g \sim \mathcal{G}$;

 6: Compute $\mathbf{x}_0 = \mathcal{F}_{\theta_k}(\mathbf{y})$, by default let $\mathbf{u}_k = \mathbf{x}_0$;

 7: Update $\mathbf{u}_{k+1} = \mathbf{u}_k - \gamma[\nabla f_{\text{mc}}(\mathbf{y}, \mathbf{A}\mathbf{u}_k) + \lambda(\mathbf{u}_k - \mathcal{F}_{\theta_k}(\mathbf{y}) - \mathbf{L}_k^{(\mathbf{y})})]$

 8: Let $\mathbf{x}_1 = \mathbf{u}_{k+1}$;

 9: Transform $\mathbf{x}_2 = T_g(\mathbf{x}_1)$;

 10: Compute $\mathbf{x}_3 = \mathcal{F}_{\theta_k}(\mathbf{A}\mathbf{x}_2)$;

 11: Update θ_{k+1} via progressively minimizing $\mathcal{L} = \mathbb{E}_{g \sim \mathcal{G}}\{\|\mathbf{x}_0 + \mathbf{L}_k^{(\mathbf{y})} - \mathbf{x}_1\|_2^2 + \alpha\|\mathbf{x}_2 - \mathbf{x}_3\|_2^2\}$ using an adaptive gradient-based optimizer (such as Adam) in each iteration;

 12: Update $\mathbf{L}_{k+1}^{(\mathbf{y})} = \mathbf{L}_k^{(\mathbf{y})} - (\mathbf{x}_1 - \mathcal{F}_{\theta_{k+1}}(\mathbf{y}))$;

 13: $k \leftarrow k + 1$

 14: **End For**

 15: **End For**

 16: **Output:** \mathcal{F}_{θ^*}

inverse problems. We extend this here to Fast Equivariant Imaging as an auxiliary primal regularization on the image domain, in the hope that joint-forcing with dual-domain EI regularization will further boost the convergence rate and generalization performance.

An alternative approach to update \mathbf{u} in **Latent-reconstruction** step of proposed FEI framework, is to include plug-and-play denoisers as proximal gradient step:

$$M_L(\mathbf{y}, \mathcal{F}_{\theta_k}) \leftarrow \mathcal{D}_\sigma(\mathbf{u}_k), \quad (22)$$

where \mathbf{u}_k is obtained by one step gradient descent of latent-reconstruction objective (e.g. (16)). and $\mathcal{D}(\cdot)$ represents classical denoisings such as BM3D (Dabov et al., 2007), DnCNN (Zhang et al., 2017), etc.

PnP-FEI generic framework

 –Initialize θ_0

 For $k = 0, 1, 2, \dots, K$

$$\left[\begin{array}{l} \text{Sample } \mathbf{y} \in \mathcal{Y}, g \sim \mathcal{G} \\ \mathbf{q}_k \leftarrow M_L(\mathbf{y}, \mathcal{F}_{\theta_k}) \\ \mathbf{u}_{k+1} \leftarrow \mathcal{D}_\sigma(\mathbf{q}_k) \quad \textit{Latent reconstruction with PnP prior} \\ \theta_{k+1} \leftarrow M_P(\mathbf{u}_{k+1}, \mathcal{F}_{\theta_k}) \quad \textit{Pseudo supervision} \end{array} \right.$$

The PnP-FEI framework summarizes the steps to be taken to apply this overall algorithm to manage the minimization of the objective of equivariant imaging. Here we present the PnP-FEI with ADMM splitting

option (Option 2), while PnP-FEI Option 1 uses the same approach with denoising steps following the gradient steps in the latent-reconstruction (we omit writing this down for the sake of avoiding repeated description).

Algorithm 3 Fast Equivariant Imaging with Plug-and-Play (PnP-FEI Option 2)

1: **Inputs:**

- \mathcal{Y} - Observations (training dataset)
- \mathbf{L} - Augmented Lagrangian multiplier
- λ - Augmented Lagrangian free parameter
- α - EI regularization parameter
- N - number of epochs
- \mathcal{G} - Group of transformations
- \mathbf{u}_0 - Initial gradient descent point of (20)
- γ - Gradient descent step size

2: **Initialize:** Neural network \mathcal{F}_θ , $\mathbf{L}_0 = \mathbf{0}$, $\mathbf{u}_0 = \mathbf{0}$, $k = 0$;

3: **For** $i = 0, \dots, N - 1$ **do:**

4: **For** $\mathbf{y} \in \mathcal{Y}$ **do:**

5: Sample T_g where $g \sim \mathcal{G}$;

6: Compute $\mathbf{x}_0 = \mathcal{F}_{\theta_k}(\mathbf{y})$, by default let $\mathbf{u}_k = \mathbf{x}_0$;

7: Update $\mathbf{u}_{k+1} = \mathcal{D}_\sigma[\mathbf{u}_k - \gamma[\nabla f_{\text{mc}}(\mathbf{y}, \mathbf{A}\mathbf{u}_k) + \lambda(\mathbf{u}_k - \mathcal{F}_{\theta_k}(\mathbf{y}) - \mathbf{L}_k^{(\mathbf{y})})]]$

8: Let $\mathbf{x}_1 = \mathbf{u}_{k+1}$;

9: Transform $\mathbf{x}_2 = T_g(\mathbf{x}_1)$;

10: Compute $\mathbf{x}_3 = \mathcal{F}_{\theta_k}(\mathbf{A}\mathbf{x}_2)$;

11: Update θ_{k+1} via progressively minimizing $\mathcal{L} = \mathbb{E}_{g \sim \mathcal{G}}\{\|\mathbf{x}_0 + \mathbf{L}_k^{(\mathbf{y})} - \mathbf{x}_1\|_2^2 + \alpha\|\mathbf{x}_2 - \mathbf{x}_3\|_2^2\}$ using an adaptive gradient-based optimizer (such as Adam) in each iteration;

12: Update $\mathbf{L}_{k+1}^{(\mathbf{y})} = \mathbf{L}_k^{(\mathbf{y})} - (\mathbf{x}_1 - \mathcal{F}_{\theta_{k+1}}(\mathbf{y}))$;

13: $k \leftarrow k + 1$

14: **End For**

15: **End For**

16: **Output:** \mathcal{F}_{θ^*}

In order to show the potential of faster reconstruction in PnP-FEI, we try to demonstrate the proximal gradient step in PnP-FEI may accelerates the reconstruction. To show this, we present some basic theoretical results in the following. We first present several assumptions crucial for our analysis.

Assumption 4.5 (Approximate projection) *We assume that the denoiser \mathcal{D} in PnP-FEI is a \mathcal{E} -optimal projection towards a manifold \mathcal{M} :*

$$\mathcal{D}(\mathbf{u}) = \mathcal{E}(\mathbf{u}) + P_{\mathcal{M}}(\mathbf{u}), \quad (23)$$

where

$$P_{\mathcal{M}}(\mathbf{u}) := \arg \min_{\mathbf{z} \in \mathcal{M}} \frac{1}{2} \|\mathbf{u} - \mathbf{z}\|_2^2, \quad (24)$$

and

$$\|\mathcal{E}(\mathbf{u})\|_2 \leq \mathcal{E}_0, \quad \forall \mathbf{u} \in \mathbb{R}^n. \quad (25)$$

In practice the image manifold \mathcal{M} typically forms a non-convex set.

Assumption 4.6 *We assume the ground truth image $\mathbf{u}^\dagger \in \mathcal{M}$, where \mathcal{M} is a closed set.*

Assumption 4.7 (Restricted Eigenvalue Condition) We define a descent cone \mathcal{C} at point \mathbf{u}^\dagger as:

$$\mathcal{C} := \{\mathbf{u} \in \mathbb{R}^n \mid \mathbf{v} = a(\mathbf{u} - \mathbf{u}^\dagger), \quad \forall a \geq 0, \mathbf{u} \in \mathcal{M}\} \quad (26)$$

and the restricted strong-convexity constant $\mu_{\mathcal{C}}$ to be the largest positive constant satisfies:

$$\mu_{\mathcal{C}} \|\mathbf{v}\|_2 \leq \|\mathbf{A}\mathbf{v}\|_2, \quad \forall \mathbf{v} \in \mathcal{C}. \quad (27)$$

The restricted eigenvalue condition is standard and crucial for robust estimation guarantee for linear inverse problem, *i.e.*, for a linear problem to be non-degenerate, this type of condition must hold (Oymak et al., 2017). We are now ready to present the main convergence result with PnP-FEI.

Theorem 4.8 Given measurements $\mathbf{y} = \mathbf{A}\mathbf{u}^\dagger + \mathbf{w}$. Let $\eta = \frac{1}{L}$ where $L = \|\mathbf{A}^T \mathbf{A}\|$, then the following bound holds for the \mathbf{u} -subproblem in PnP-FEI (at K -th iteration) utilizing proximal gradient denoiser:

$$\mathbb{E} \|\mathbf{u}_{K+1} - \mathbf{u}^\dagger\|_2 \leq \alpha^K \cdot \|\mathbf{u}_0 - \mathbf{u}^\dagger\|_2 + \frac{1 - \alpha^K}{1 - \alpha} \left(\frac{\kappa(\sum_{k=1}^K \lambda \delta_k + \epsilon)}{L} + \mathcal{E}_0 \right), \quad (28)$$

where $\kappa = 1$ if \mathcal{C} is convex, $\kappa = 2$ if \mathcal{C} is nonconvex, and:

$$\alpha := \kappa \sqrt{\left(1 - \frac{\lambda}{L}\right) \left(1 - \frac{\lambda + \mu_{\mathcal{C}}}{L}\right)}, \quad (29)$$

$$\delta_k := \mathbb{E} \sup_{\mathbf{v} \in \mathcal{C} \cap \mathcal{B}^n} \mathbf{v}^T \left(\mathcal{F}_{\theta_k}(\mathbf{y}) - \mathbf{u}^\dagger \right), \quad (30)$$

$$\epsilon := \mathbb{E} \sup_{\mathbf{v} \in \mathcal{C} \cap \mathcal{B}^n} \mathbf{v}^T \mathbf{A}^T \mathbf{w}. \quad (31)$$

Proof See Appendix. ■

Remark 1 The convergence of PnP-FEI are critically dependent on the penalty parameter λ ; notably, with a suitable choice of λ , the method exhibits significantly faster convergence rates compared to its standard FEI counterpart, as demonstrated by the numerical experiments in Sec. 5.

Remark 2 The error term δ_k scales directly with the reconstruction accuracy $\mathcal{F}_{\theta_k}(\mathbf{y}) - \mathbf{u}^\dagger$, implying that as the estimator improves during training, δ_k diminishes monotonically.

4.4 Test Time Efficient Adaptation of FEI

Equivariant Imaging (EI) is applicable not only to unsupervised learning but also to Test-Time Adaptation (TTA) (Wang et al., 2024). Given the strict time constraints inherent in Test-Time Adaptation, the proposed FEI framework is a compelling candidate for accelerating the adaptation process, particularly in scenarios where EI is employed.

Let $\hat{\theta}$ denote the learned parameters of a pre-trained model. For a specific test instance $(\hat{\mathbf{y}}, \hat{\mathbf{A}})$, we initialize $\theta_0 = \hat{\theta}$ and iteratively fine-tune the model parameters using the alternating FEI scheme for T iterations:

$$\begin{cases} \mathbf{u} \leftarrow M_L(\hat{\mathbf{y}}, \mathcal{F}_\theta) \\ \theta \leftarrow M_P(\mathbf{u}, \mathcal{F}_\theta) \end{cases} \quad (32)$$

where M_L and M_P correspond to the Latent reconstruction (Eq. 16) and Pseudo supervision (Eq. 17) updates, respectively. Once done, the final adaptation is given by

$$\hat{\mathbf{x}} = \mathcal{F}_\theta(\hat{\mathbf{y}})$$

with the adapted parameters θ . As we will see, our FEI framework is particularly effective in test-time model adaptation, ensuring improved imaging accuracy and robustness against distribution shifts.

5. Numerical Experiments

We assess the effectiveness of the proposed framework using experiments conducted on different inverse problems. The inverse problems we consider are sparse-view CT and inpainting. The configuration is as follows:

(a) Metric To evaluate reconstruction quality, we report standard PSNR and SSIM metrics. Additionally, we adopt the equivariance metric proposed by Chaman and Dokmanić (2021) to quantify the equivariance properties of the estimator. This metric measures the mean squared error deviation from the canonical equivariance constraint $T_g G_\theta(\mathbf{A}\mathbf{x}) = G_\theta(\mathbf{A}T_g\mathbf{x})$, expressed in dB:

$$\text{EQUIV} = -10 \log \left(\mathbb{E}_g \left\{ \|T_g \mathcal{F}_\theta(\mathbf{A}\mathbf{x}) - \mathcal{F}_\theta(\mathbf{A}T_g\mathbf{x})\|_2^2 \right\} \right), \quad (33)$$

Intuitively, this metric functions as a PSNR analogue specifically for quantifying equivariance.

(b) Neural Network We use the same U-Net to build G_θ as suggested in Chen et al. (2021) for EI, FEI and PnP-FEI. Specifically, G_θ is a four-depth residual U-Net (Ronneberger et al., 2015) with a symmetric encoder-decoder and long skip connections. Each encoder comprises two 3×3 Convolution-BatchNorm-ReLU blocks with identity shortcuts, followed by 2×2 max pooling to double channels [64, 128, 256, 512]. The decoder mirrors the encoder in a refinement manner, and a final 1×1 convolution restores the output. For the measurement consistency loss, for simplicity, we choose ℓ_2 in this experiment.

(c) Baselines For the training phase, we benchmark our proposed FEI scheme against: (i) standard EI; and (ii) PnP-FEI instantiated with a pre-trained DnCNN denoiser (see Table 1). We set the noise standard deviation to $\sigma = 0.01$ and utilize the implementations provided by the `DeepInv` library¹. To ensure reproducibility and fairness, all EI results were generated using the official source code released by Chen et al. (2021). Regarding Test-Time Adaptation (TTA), we evaluate the proposed approach against three distinct strategies: (i) Standard Test-Time Training (TTT) (Darestani et al., 2022), which relies solely on measurement consistency loss; (ii) A modified AdaptNet (Zhao et al., 2024), where we integrate the original lightweight adaptive layer into our U-Net backbone, optimizing it via equivariant loss to maintain architectural consistency; and (iii) our proposed FEI adaptation strategy.

(d) Initialization For consistency, all learnable weights are initialized following the protocol of Chen et al. (2021). In the proposed FEI framework for sparse-view CT, we configure the hyperparameters as follows: Lagrangian multiplier $\lambda = 1$, NAG momentum $\beta = 0.1$, step size $\eta = 0.01$, and inner iterations $J = 10$. Conversely, for the image inpainting task, we set $\lambda = 0.1$, $\beta = 0.9$, $\eta = 0.09$, and maintain $J = 10$.

1. <https://deepinv.github.io/deepinv/>

Framework	Learning strategy	Description
EI	Adam	Vanilla EI framework, which use back-propagation and end-to-end training strategy.
FEI-Option1	Inexact HQS	HQS with accelerated gradient descent to approximately minimize Latent-reconstruction step subproblem, while Adam for online Pseudo-supervision, Algorithm 1.
FEI-Option2	Modified ADMM	The difference from FEI-Option1 is the change of splitting style to linearized ADMM, with gradient step for Latent-reconstruction, while Adam for online Pseudo-supervision, Algorithm 3.
PnP-FEI	Proximal Gradient	The difference from FEI is the use of pre-trained denoiser for Latent-reconstruction step.

Table 1: Unsupervised learning algorithms in our experiments.

(e) Training For sparse-view CT, we utilize the Adam optimizer initialized with a learning rate of 1×10^{-3} , adhering to the decay schedule outlined in Chen et al. (2021). We train the models for 5,000 epochs, employing a batch size of 8 and an equivariance strength $\alpha = 1000$ to balance performance and efficiency. For the image inpainting task, we maintain the initial learning rate at 1×10^{-3} with a total training duration of 2,000 epochs. We configure the batch size to 4 and set the equivariance strength to $\alpha = 1.0$. To enhance stability, we adopt the moving average technique from Sun et al. (2021) to smooth the reconstructed outputs. Finally, we implement early stopping with a patience of 300 epochs to mitigate overfitting.

(f) Adaptation We evaluate the proposed approach on sparse-view CT images for TTA task, under two distinct conditions: minor distribution shifts and severe out-of-distribution (OOD) scenarios. We utilize a publicly available pre-trained model trained within the EI framework. Specifically, we employ the model from the original study by Chen et al. (2021), which was trained on 90 clean samples from the CT-100 dataset for $T = 5000$ epochs using the Adam optimizer with a constant learning rate of 5×10^{-4} . The adaptation process utilizes the Adam optimizer with a fixed learning rate of 1×10^{-3} for $T = 100$ epochs following the procedure in Zhao et al. (2024); Quan et al. (2022).

5.1 Sparse-view CT

The forward operator \mathbf{A} for sparse-view CT is modeled as the Radon transform, where 50 projection angles are uniformly subsampled to generate sparse-view sinograms (observations) \mathbf{y} . The transformation group G employed for equivariance consists of 2D planar rotations, implemented by sampling random angles from the full 360° range. For the dataset, we utilize 90 images sampled from the CT100 (Clark et al., 2013) dataset for training. The remaining 10 images, processed with the same scanning geometry, are reserved to evaluate the generalization performance of the trained models. All images are resized to a resolution of 128×128 (16384) pixels.

To evaluate the efficiency gains of the proposed FEI scheme for sparse-view CT imaging, we show the PSNR curves with respect to both iterations and times in Figure 2. Notably, FEI achieves an order-of-magnitude ($\geq 10\times$) acceleration over standard EI training. Despite the inexact nature of the latent variable update, FEI exhibits a smooth and monotonic convergence trajectory similar to the exact EI baseline. This

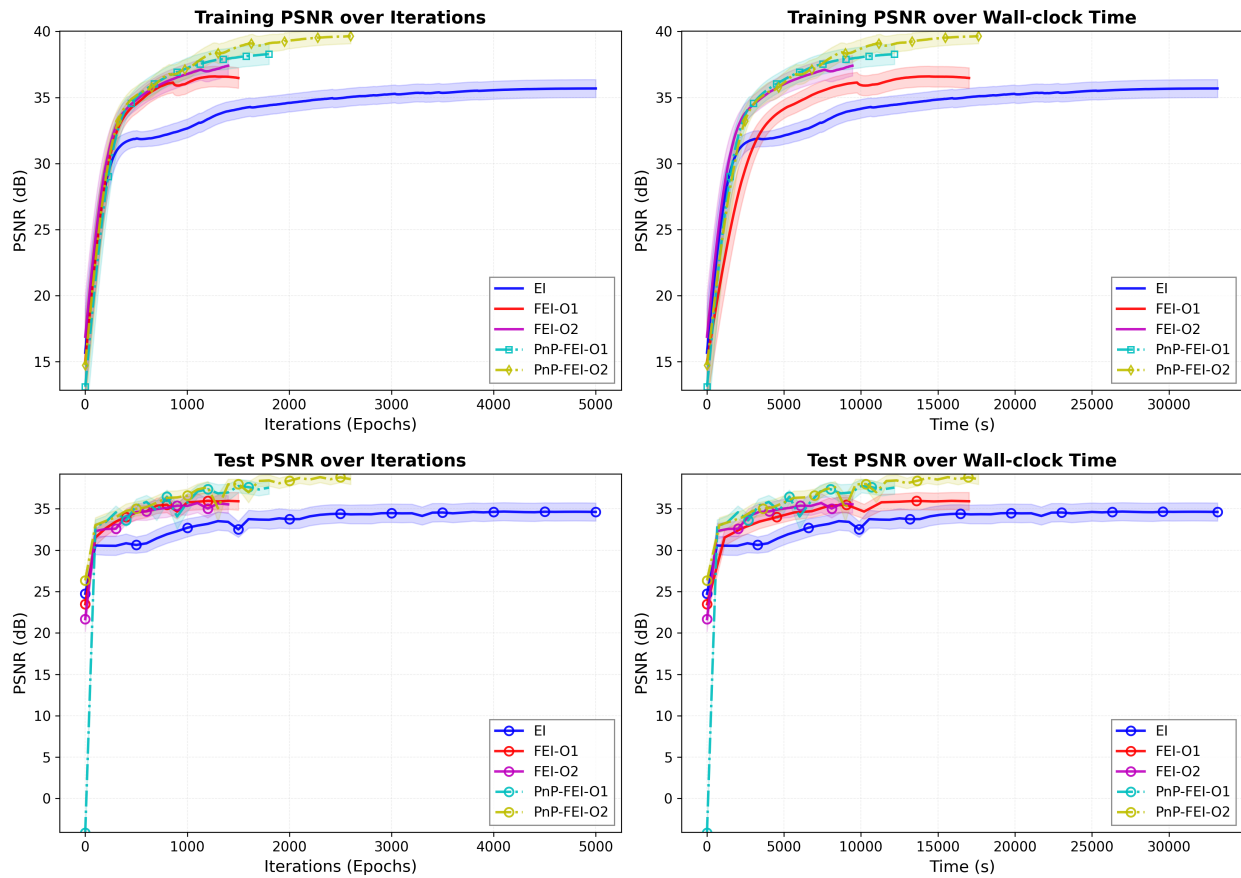


Figure 2: PSNR and MSE curves with respect to iteration and time for Sparse-view CT reconstruction. We observe a 10-time acceleration can be achieved by FEI over EI.

empirically validates that the approximation error introduced by our relaxed splitting does not destabilize the optimization process. Furthermore, Table 2 and Figure 3 show that networks trained via our FEI and PnP-FEI strategies exhibit superior generalization performance compared to standard EI baselines.

Method	PSNR \uparrow	SSIM \uparrow
Supervised	38.17 ± 1.57	0.9689 ± 0.0073
PnP-FEI-O2	37.56 ± 1.33	0.9648 ± 0.0053
PnP-FEI-O1	37.35 ± 1.43	0.9666 ± 0.0054
FEI-O1	36.17 ± 1.44	0.9579 ± 0.0065
FEI-O2	35.94 ± 1.65	0.9528 ± 0.0093
EI	35.03 ± 1.53	0.9531 ± 0.0067
FBP	30.24 ± 1.33	0.8335 ± 0.0341

Table 2: Averaged PSNR and SSIM on testing dataset for sparse-view CT reconstruction.

5.2 Image Inpainting

The mask rate for the inpainting task is 0.6, which means 60% of pixels are randomly removed. Here we choose random shift as the transformation. The dataset we used here is Urban100 (Huang et al., 2015) which is the same as Chen et al. (2021). For each image, we cropped a 512×512 pixel area in the center and then resized it to 256×256 (65536 pixels) for the ground truth image. The first 90 measurements are for training, while the last 10 images are for testing. Figure 4 demonstrates significantly faster convergence compared to the vanilla EI method. Furthermore, Table 3 and Figure 5 indicate that the FEI-based approach achieves superior generalization performance relative to the standard EI method.

Method	PSNR \uparrow	SSIM \uparrow
Supervised	22.65 ± 2.15	0.8928 ± 0.0434
PnP-FEI-O1	23.56 ± 2.56	0.9116 ± 0.0482
PnP-FEI-O2	22.25 ± 2.41	0.8913 ± 0.0559
FEI-O1	22.75 ± 2.22	0.9043 ± 0.0500
FEI-O2	22.64 ± 2.38	0.8971 ± 0.0522
EI	21.49 ± 2.30	0.8733 ± 0.0650
Masked	2.84 ± 1.57	0.1196 ± 0.0241

Table 3: Averaged PSNR and SSIM on testing dataset for imaging inpainting.

5.3 Additional Analysis on Test-Time Model Adaptation

In this section, we evaluate the proposed FEI framework for TTA with sparse-view CT reconstruction task. Considering the practical applications, in the following experiments, we assume that the noise distribution is mixed Poisson-Gaussian, i.e.,

$$\mathbf{y} = \gamma \mathcal{P}\left(\frac{\mathbf{x}}{\gamma}\right) + \sigma \epsilon, \tag{34}$$

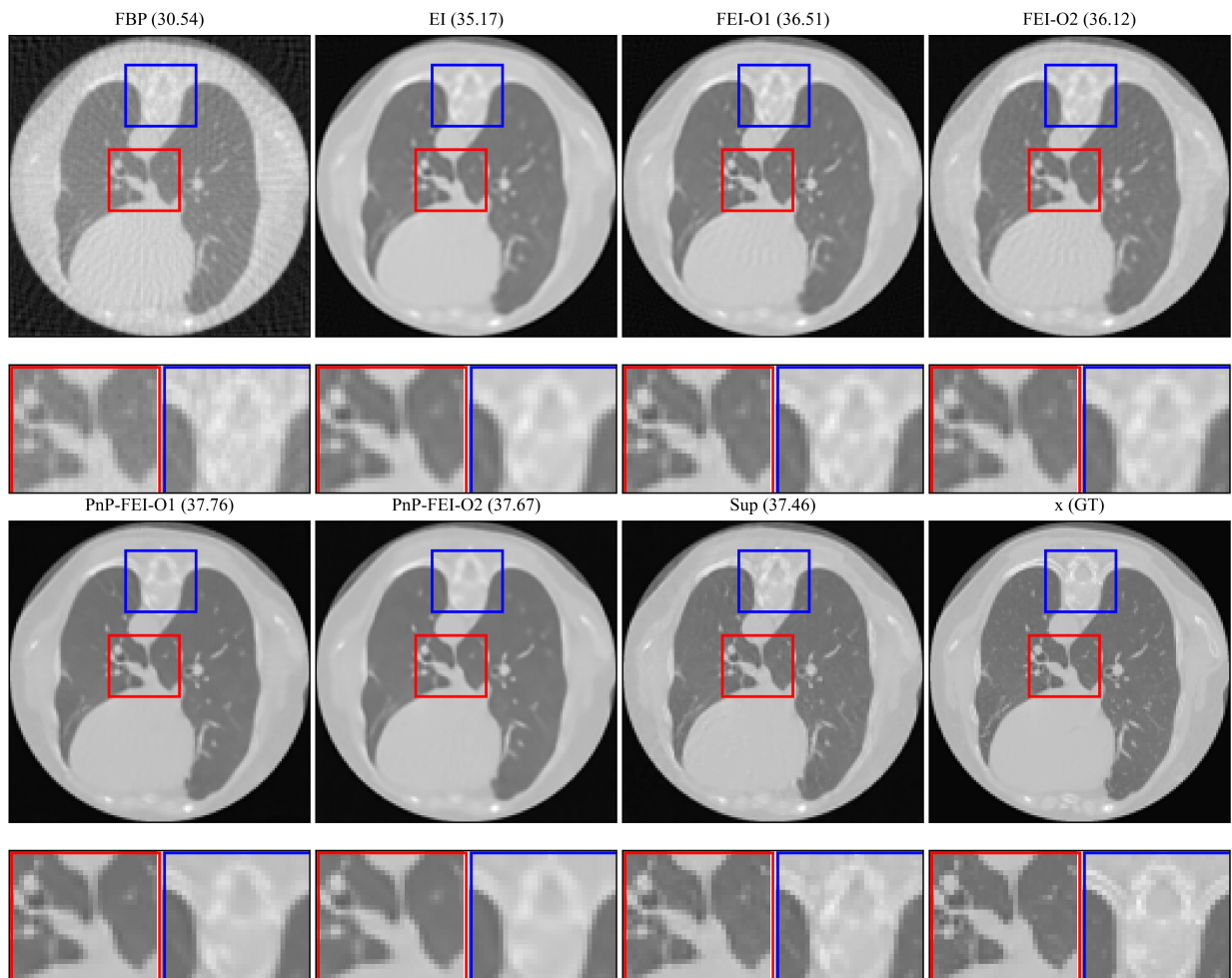


Figure 3: Visualization of test sample for sparse-view CT reconstruction.

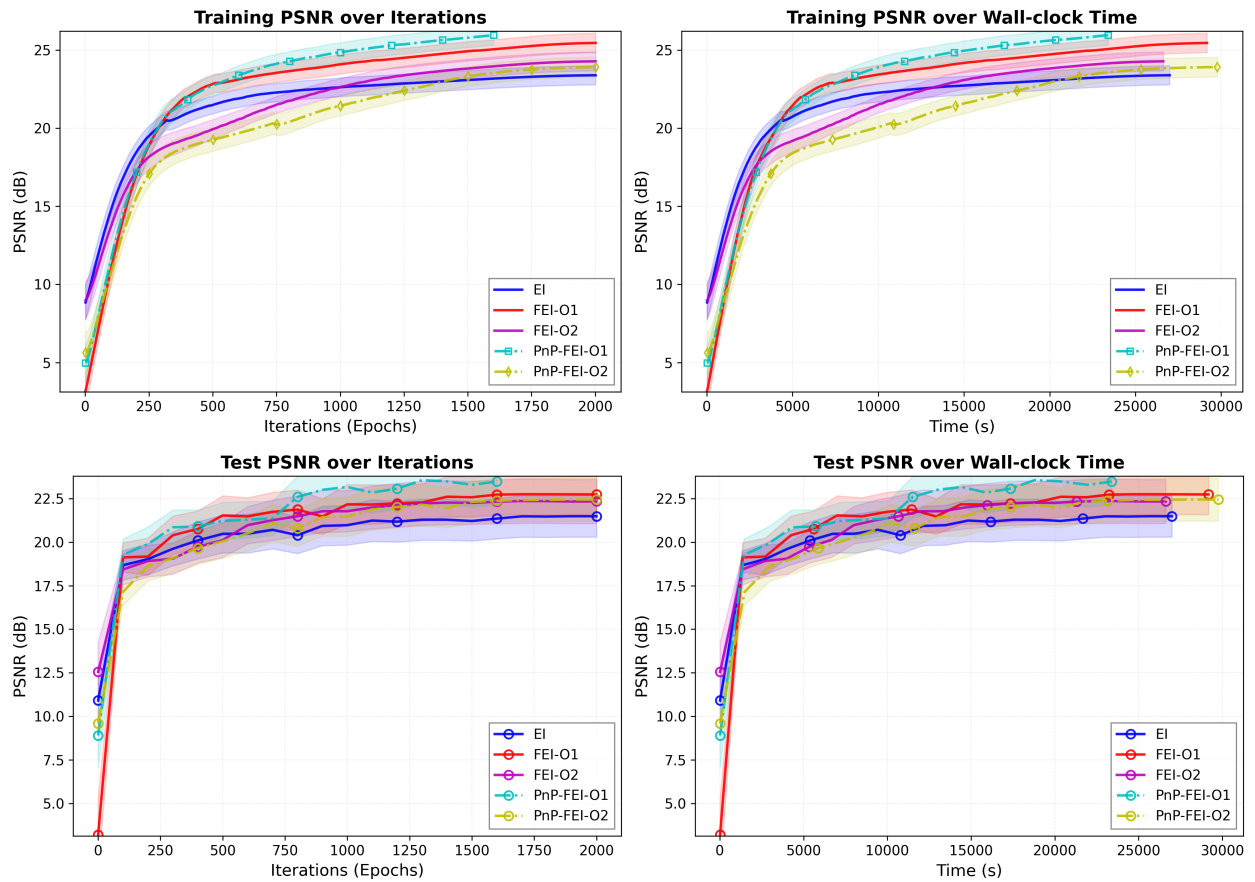


Figure 4: PSNR and MSE curves with respect to iteration and time for image inpainting. We observe an significant acceleration can be achieved by FEI over EI.

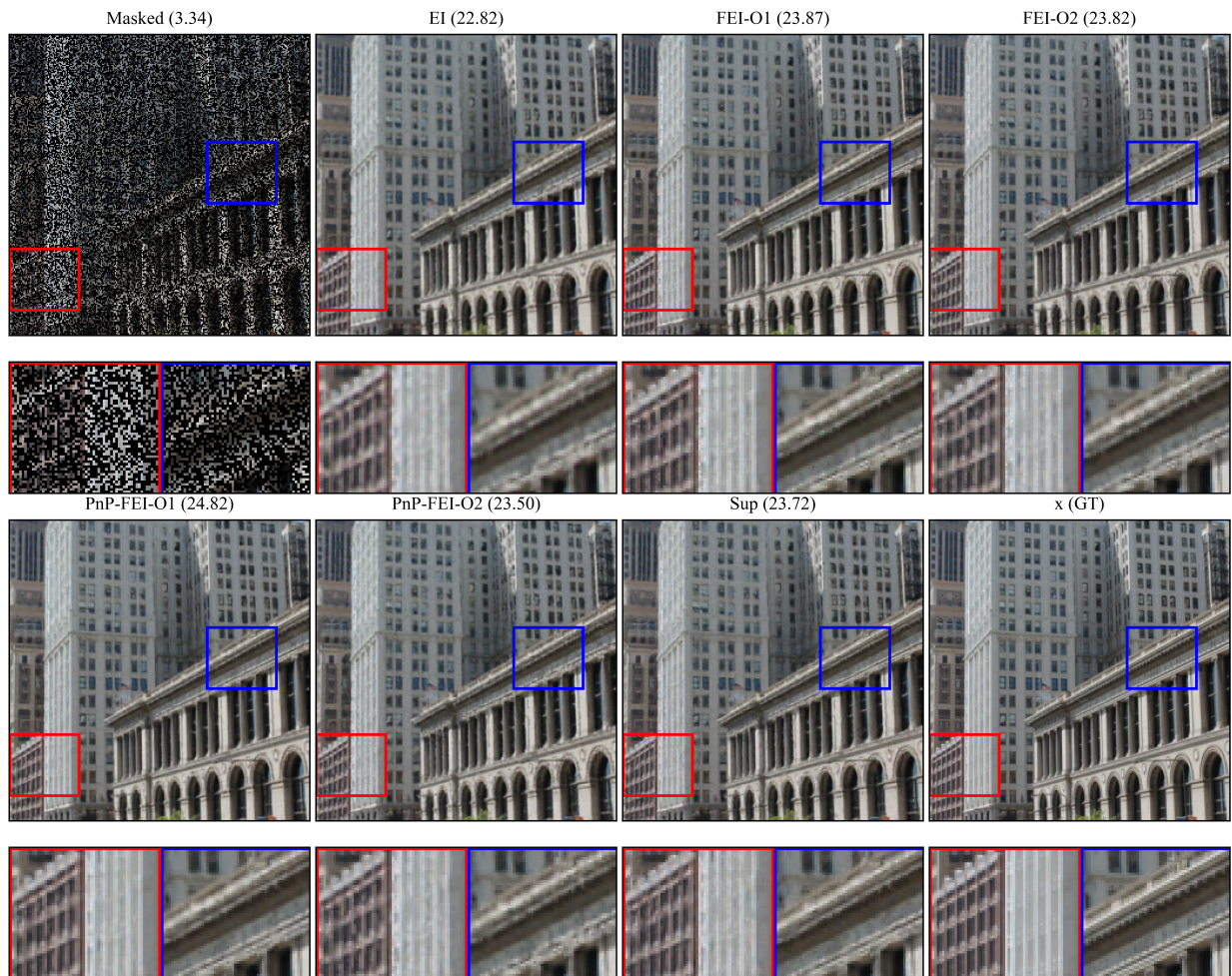


Figure 5: Visualization of test sample for imaging inpainting.

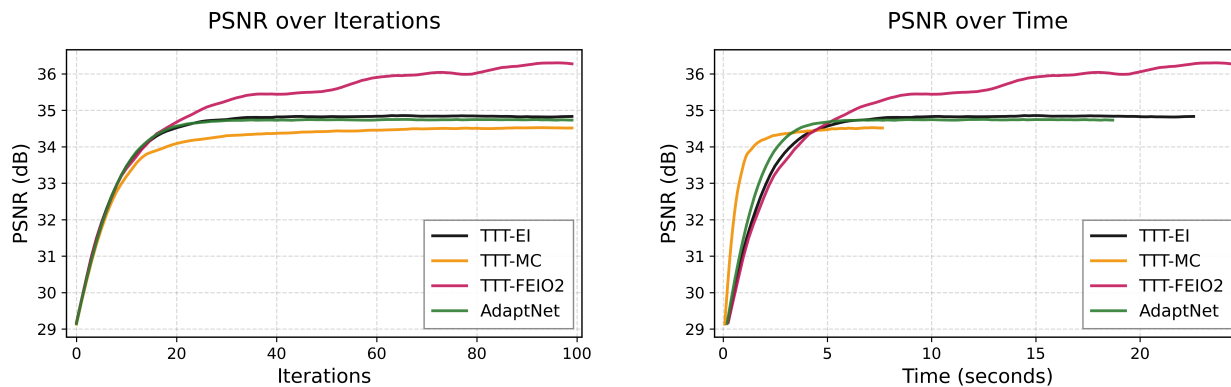
where \mathcal{P} denotes the Poisson distribution, and $\epsilon \in \mathcal{N}(\mathbf{0}, \mathbf{I})$.

To evaluate the efficacy of the proposed method in Test-Time Adaptation (TTA), we conducted comparative experiments across two distinct scenarios. First, to assess robustness against mild distribution shifts, we benchmarked various adaptation methods under varying noise intensities. As shown in Table 4 and Figure 6, FEI demonstrates superior adaptation capabilities under minor shifts; it achieves state-of-the-art reconstruction performance while maintaining competitive computational efficiency. Even as noise intensity escalates, FEI consistently delivers high-fidelity reconstructions, underscoring its robustness in low-shift regimes.

Subsequently, to rigorously evaluate FEI under significant distribution shifts, we extended our comparison to scenarios involving substantial domain discrepancies. Specifically, we defined the source domain \mathcal{S} and target domain \mathcal{D} for three specific shifts: 1) *Anatomy shift*, where \mathcal{S} comprises body (lung and abdomen) CT images collected from Mayo at 50 views, and \mathcal{D} consists of brain CT images from the same setting; 2) *Dataset shift*, where \mathcal{S} denotes body images from Mayo, and \mathcal{D} represents the SARS-COV2 dataset; and 3) *Ratio shift*, where \mathcal{S} contains body images from Mayo at 50 views, while \mathcal{D} contains body images from Mayo at 25 views. As can be seen from Table 5 and Figure 7, FEI achieves superior performance against other methods across all three domain shift scenarios.

Noise	σ, γ	Classic	Unsupervised			TTT*	Network Adaptation		
		FBP	Pre-trained	REI (known σ, γ) (Chen et al., 2022)	EI-UNSURE (unknown σ, γ) (Tachella et al., 2024)	MC (unknown σ, γ) (Darestani et al., 2022)	EI (unknown σ, γ) (Chen et al., 2021)	AdaptNet (unknown σ, γ) (Zhao et al., 2024)	FEI-O2 (unknown σ, γ)
MPG	5×10^{-3}	25.55 ± 0.83	30.26 ± 1.19	32.93 ± 0.69	30.88 ± 0.70	34.47 ± 1.02	34.71 ± 0.95	34.74 ± 1.12	36.04 ± 1.41
	1×10^{-2}	23.49 ± 1.13	28.10 ± 1.43	30.78 ± 0.66	28.11 ± 0.82	33.65 ± 0.88	33.70 ± 0.91	33.50 ± 1.06	34.95 ± 0.88
	5×10^{-2}	17.44 ± 1.57	22.02 ± 1.86	28.46 ± 0.75	22.42 ± 0.92	30.35 ± 0.80	31.30 ± 0.82	29.12 ± 1.15	31.26 ± 0.78

Table 4: Mean PSNR values of sparse-view CT reconstructions with different noise levels for TTA. Pre-trained model here is the pre-trained model with the same backbone as EI. The best performance is highlighted in **bold**.



(a) Mean PSNR values vs. epochs.

(b) Mean PSNR values vs. Avg. wall clock time.

Figure 6: PSNR curves vs. iteration numbers and time during adaptation for different methods.

Algorithm	Setup	Methods	Anatomy Shift	Dataset Shift	Ratio Shift
			\mathcal{S} : Body \mathcal{D} : Brain	\mathcal{S} : Mayo \mathcal{D} : SARS	\mathcal{S} : 50 views \mathcal{D} : 25 views
FBP	-	-	30.01 ± 1.12	20.41 ± 0.87	24.78 ± 1.45
Pre-trained	Train on \mathcal{S} Test on \mathcal{D}	UNet	35.71 ± 1.45	24.85 ± 1.34	27.02 ± 1.49
MC	Train on \mathcal{S} TTA on \mathcal{D}	UNet	35.12 ± 1.77	31.14 ± 2.04	30.45 ± 1.76
EI	Train on \mathcal{S} TTA on \mathcal{D}	UNet	35.98 ± 1.61	32.84 ± 2.20	32.02 ± 1.41
EI	Train on \mathcal{S} TTA on \mathcal{D}	AdaptNet	35.54 ± 1.36	23.78 ± 1.34	28.00 ± 1.61
FEI-O1	Train on \mathcal{S} TTA on \mathcal{D}	UNet	37.82 ± 1.23	33.42 ± 1.74	32.23 ± 1.50

Table 5: Mean PSNR values of sparse-view CT across three domain shift scenarios with different adaptation approaches. The best is highlighted in **bold**.

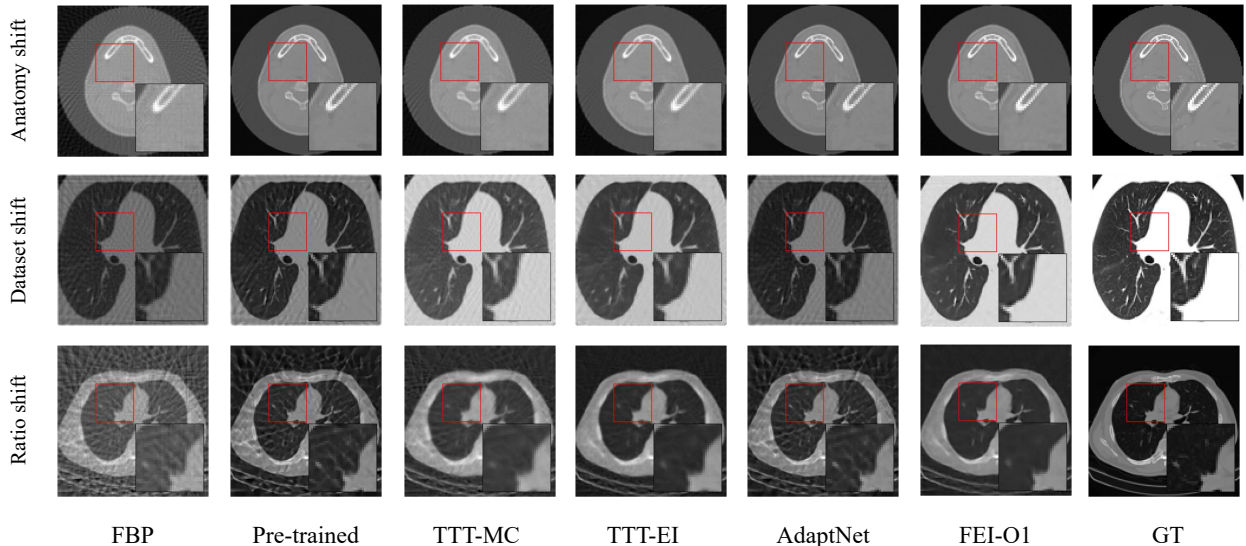


Figure 7: Visualization results of different adaptation approaches across three domain shift scenarios.

6. Conclusion

We propose FEI and its variant PnP-FEI for accelerating unsupervised training of deep neural networks to imaging inverse problems without the need of ground-truth data. We observe that our framework is capable of significantly accelerating the state-of-the-art unsupervised training scheme Equivariant Imaging proposed by (Chen et al., 2021), along with improved generalization performance and boosted adaptation performance. We believe that this work is crucial for the area of deep learning for computational imaging,

via making the unsupervised training truly practical. Our algorithmic framework (Augmented Lagrangian plus PnP) can be easily extended to more recent variants of EI such as Robust Equivariant Imaging (REI) (Chen et al., 2022), Multi-Operator Imaging (MOI) (Tachella et al., 2022), and our Sketched Equivariant Imaging (SkEI) (Xu et al., 2024), etc.

7. Appendix

7.1 Proof of Proposition 4.3

Proposition 4.3 (Convergence of Inexact Latent Step) *If FEI iteration is performed using step size $\eta = 1/2L$ with $\mathbf{u}_{t+1} = \mathbf{u}_t - \eta g(\mathbf{u}_t)$, then the decrease in the objective function value $F(\mathbf{u})$ satisfies:*

$$F(\mathbf{u}_{t+1}) \leq F(\mathbf{u}_t) - \frac{1}{8L} \|\nabla\Phi(\mathbf{u}_t)\|^2 + \frac{1}{4L} \delta_t^2.$$

Proof For F , use descent lemma:

$$F(\mathbf{u}_{k+1}) \leq F(\mathbf{u}_k) + \langle \nabla F(\mathbf{u}_k), \mathbf{u}_{k+1} - \mathbf{u}_k \rangle + \frac{L}{2} \|\mathbf{u}_{k+1} - \mathbf{u}_k\|^2, \quad (35)$$

then with the update $\mathbf{u}_{k+1} - \mathbf{u}_k = -\eta \nabla\Phi(\mathbf{u}_k)$, we can get

$$F(\mathbf{u}_{k+1}) \leq F(\mathbf{u}_k) - \eta \langle \nabla F(\mathbf{u}_k), \nabla\Phi(\mathbf{u}_k) \rangle + \frac{L\eta^2}{2} \|\nabla\Phi(\mathbf{u}_k)\|^2, \quad (36)$$

unfold $\nabla F = \nabla\Phi + \nabla\Psi$, then we have

$$\langle \nabla F, \nabla\Phi \rangle = \|\nabla\Phi\|^2 + \langle \nabla\Psi, \nabla\Phi \rangle, \quad (37)$$

plug Eq. (37) into relation (36), we have

$$F(\mathbf{u}_{k+1}) \leq F(\mathbf{u}_k) - \eta \|\nabla\Phi\|^2 - \eta \langle \nabla\Psi, \nabla\Phi \rangle + \frac{L\eta^2}{2} \|\nabla\Phi\|^2, \quad (38)$$

and

$$F(\mathbf{u}_{k+1}) \leq F(\mathbf{u}_k) - \left(\eta - \frac{L\eta^2}{2} \right) \|\nabla\Phi(\mathbf{u}_k)\|^2 - \eta \langle \nabla\Psi(\mathbf{u}_k), \nabla\Phi(\mathbf{u}_k) \rangle, \quad (39)$$

then use Cauchy-Schwarz and Young's Inequality,

$$-\eta \langle \nabla\Psi(\mathbf{u}_k), \nabla\Phi(\mathbf{u}_k) \rangle \leq \eta \|\nabla\Psi(\mathbf{u}_k)\| \|\nabla\Phi(\mathbf{u}_k)\| \leq \frac{\eta}{2} \|\nabla\Psi(\mathbf{u}_k)\|^2 + \frac{\eta}{2} \|\nabla\Phi(\mathbf{u}_k)\|^2, \quad (40)$$

combine this relation with relation (39), we can get

$$F(\mathbf{u}_{k+1}) \leq F(\mathbf{u}_k) - \left(\eta - \frac{L\eta^2}{2} \right) \|\nabla\Phi(\mathbf{u}_k)\|^2 + \frac{\eta}{2} \|\nabla\Phi(\mathbf{u}_k)\|^2 + \frac{\eta}{2} \|\nabla\Psi(\mathbf{u}_k)\|^2$$

$$F(\mathbf{u}_{k+1}) \leq F(\mathbf{u}_k) - \left(\frac{\eta}{2} - \frac{L\eta^2}{2} \right) \|\nabla\Phi(\mathbf{u}_k)\|^2 + \frac{\eta}{2} \|\nabla\Psi(\mathbf{u}_k)\|^2$$

taking $\eta = \frac{1}{2L}$ results in

$$F(\mathbf{u}_{k+1}) \leq F(\mathbf{u}_k) - \frac{1}{8L} \|\nabla\Phi(\mathbf{u}_k)\|^2 + \frac{1}{4L} \delta_k^2,$$

this finish the proof. ■

7.2 Proof of Theorem 4.4

Before present the proof of main theorem, we first show a useful lemma.

Lemma 7.1 (Inexact Descent Lemma) *Suppose that the objective F is L -smooth, with the inexact update $\mathbf{u}_{k+1} - \mathbf{u}_k = -\eta\nabla\Phi(\mathbf{u}_k)$, and $\eta < \frac{1}{L}$, we have*

$$F(\mathbf{u}_{k+1}) \leq F(\mathbf{u}_k) - c\|\mathbf{u}_{k+1} - \mathbf{u}_k\|^2 + \frac{1}{2L}\|e(\mathbf{u}_k)\|^2$$

where $c = \left(\frac{1}{\eta} - L\right) > 0$ and $e(\mathbf{u}) = \nabla\Psi(\mathbf{u})$ as defined in Eq. (9).

Proof Since F is L -smooth, we have

$$F(y) \leq F(x) + \langle \nabla F(x), y - x \rangle + \frac{L}{2}\|y - x\|^2, \quad \forall x, y$$

let $x = \mathbf{u}_k$ and $y = \mathbf{u}_{k+1}$, we have

$$F(\mathbf{u}_{k+1}) \leq F(\mathbf{u}_k) + \langle \nabla F(\mathbf{u}_k), \mathbf{u}_{k+1} - \mathbf{u}_k \rangle + \frac{L}{2}\|\mathbf{u}_{k+1} - \mathbf{u}_k\|^2, \quad (41)$$

since $\mathbf{u}_{k+1} - \mathbf{u}_k = -\eta\nabla\Phi(\mathbf{u}_k)$, we can obtain the following equivalent form of ∇F as:

$$\nabla F(\mathbf{u}_k) = \nabla\Phi(\mathbf{u}_k) + e(\mathbf{u}_k) = -\frac{1}{\eta}(\mathbf{u}_{k+1} - \mathbf{u}_k) + e(\mathbf{u}_k), \quad (42)$$

combine Eq. (42) with relation (41), we have

$$\begin{aligned} \langle \nabla F(\mathbf{u}_k), \mathbf{u}_{k+1} - \mathbf{u}_k \rangle &= \left\langle -\frac{1}{\eta}(\mathbf{u}_{k+1} - \mathbf{u}_k) + e(\mathbf{u}_k), \mathbf{u}_{k+1} - \mathbf{u}_k \right\rangle \\ &= -\frac{1}{\eta}\|\mathbf{u}_{k+1} - \mathbf{u}_k\|^2 + \langle e(\mathbf{u}_k), \mathbf{u}_{k+1} - \mathbf{u}_k \rangle \end{aligned}$$

using Young's Inequality with $\rho > 0$,

$$\langle e(\mathbf{u}_k), \mathbf{u}_{k+1} - \mathbf{u}_k \rangle \leq \frac{1}{2\rho}\|e(\mathbf{u}_k)\|^2 + \frac{\rho}{2}\|\mathbf{u}_{k+1} - \mathbf{u}_k\|^2, \quad (43)$$

combine above relations with relation (41), we have

$$F(\mathbf{u}_{k+1}) \leq F(\mathbf{u}_k) - \left(\frac{1}{\eta} - \frac{L}{2} - \frac{\rho}{2}\right)\|\mathbf{u}_{k+1} - \mathbf{u}_k\|^2 + \frac{1}{2\rho}\|e(\mathbf{u}_k)\|^2,$$

taking $\rho = L$ and $\eta < \frac{1}{L}$, we have

$$F(\mathbf{u}_{k+1}) \leq F(\mathbf{u}_k) - \left(\frac{1}{\eta} - L\right)\|\mathbf{u}_{k+1} - \mathbf{u}_k\|^2 + \frac{1}{2L}\|e(\mathbf{u}_k)\|^2, \quad (44)$$

this finish the proof. ■

Theorem 4.4 (Global Asymptotic Convergence to an Error Neighborhood) *Suppose Assumptions 4.1 and Assumption 4.2 hold. Let the step size be set to $\eta = \frac{1}{L}$. Then, the sequence $\{\mathbf{u}_k\}$ generated by the FEI latent reconstruction step satisfies:*

$$\liminf_{k \rightarrow \infty} \|\nabla F(\mathbf{u}_k)\|^2 \leq \delta_\infty^2.$$

This implies that the algorithm converges to an neighborhood of the critical point of $F(\mathbf{u})$, where the radius of the neighborhood is determined by the asymptotic magnitude of the equivariance gradient error δ_∞ .

Proof From Lemma 7.1, we have

$$F(\mathbf{u}_{k+1}) \leq F(\mathbf{u}_k) - \left(\frac{1}{\eta} - L\right) \|\mathbf{u}_{k+1} - \mathbf{u}_k\|^2 + \frac{1}{2L} \|e(\mathbf{u}_k)\|^2, \quad (45)$$

summarize it from $k = 0$ to K , we have

$$\sum_{k=0}^K (F(\mathbf{u}_{k+1}) - F(\mathbf{u}_k)) \leq \sum_{k=0}^K \left(-c \|\mathbf{u}_{k+1} - \mathbf{u}_k\|^2 + \frac{1}{2L} \|e(\mathbf{u}_k)\|^2 \right) \quad (46)$$

$$c \sum_{k=0}^K \|\mathbf{u}_{k+1} - \mathbf{u}_k\|^2 \leq F(\mathbf{u}_0) - F(\mathbf{u}_{K+1}) + \frac{1}{2L} \sum_{k=0}^K \|e(\mathbf{u}_k)\|^2, \quad (47)$$

since $\mathbf{u}_{k+1} - \mathbf{u}_k = \nabla F(\mathbf{u}_k)$, rearranging the inequality

$$c \sum_{k=0}^K \|\nabla F(\mathbf{u}_k)\|^2 \leq F(\mathbf{u}_0) - F(\mathbf{u}_{K+1}) + \frac{1}{2L} \sum_{k=0}^K \|e(\mathbf{u}_k)\|^2, \quad (48)$$

Since F is bounded below by F_{\min} , we have

$$F(\mathbf{u}_0) - F(\mathbf{u}_{K+1}) \leq F(\mathbf{u}_0) - F_{\min} := C_F < \infty, \quad (49)$$

thus,

$$\sum_{k=0}^K \|\nabla F(\mathbf{u}_k)\|^2 \leq \frac{C_F}{c} + \frac{1}{2Lc} \sum_{k=0}^K \|e(\mathbf{u}_k)\|^2. \quad (50)$$

Dividing both sides by $K + 1$:

$$\frac{1}{K+1} \sum_{k=0}^K \|\nabla F(\mathbf{u}_k)\|^2 \leq \frac{C_F}{c(K+1)} + \frac{1}{2Lc(K+1)} \sum_{k=0}^K \|e(\mathbf{u}_k)\|^2. \quad (51)$$

Taking the limit inferior as $K \rightarrow \infty$: The first term on the RHS vanishes: $\lim_{K \rightarrow \infty} \frac{C_F}{c(K+1)} = 0$. For the second term, using Assumption 4.2 ($\|e(\mathbf{u}_k)\| \leq \delta_k$), we have:

$$\liminf_{K \rightarrow \infty} \frac{1}{K+1} \sum_{k=0}^K \|\nabla F(\mathbf{u}_k)\|^2 \leq \limsup_{K \rightarrow \infty} \frac{1}{K+1} \sum_{k=0}^K \delta_k^2. \quad (52)$$

Since $\limsup_{k \rightarrow \infty} \delta_k \leq \delta_\infty$, it follows that the Cesaro mean of the squared errors is bounded by δ_∞^2 . Finally we can conclude:

$$\liminf_{k \rightarrow \infty} \|\nabla F(\mathbf{u}_k)\|^2 \leq \delta_\infty^2, \quad (53)$$

this finish the proof. ■

7.3 Proof of Theorem 4.8

This section is mainly focus on the theoretical analysis of PnP-FEI which utilizing both primal and dual priors for unsupervised learning. From this motivational analysis, our aim is to demonstrate the potentially faster reconstruction guarantee of PnP-FEI compared to FEI-based methods.

Theorem 4.8 *Given measurements $\mathbf{y} = \mathbf{A}\mathbf{u}^\dagger + \mathbf{w}$. Let $\eta = \frac{1}{L}$ where $L = \|\mathbf{A}^T\mathbf{A}\|$, then the following bound holds for the \mathbf{u} -subproblem in PnP-FEI (at K -th iteration) utilizing proximal gradient denoiser:*

$$\mathbb{E}\|\mathbf{u}_{K+1} - \mathbf{u}^\dagger\|_2 \leq \alpha^K \cdot \|\mathbf{u}_0 - \mathbf{u}^\dagger\|_2 + \frac{1 - \alpha^K}{1 - \alpha} \left(\frac{\kappa(\sum_{k=1}^K \lambda\delta_k + \epsilon)}{L} + \mathcal{E}_0 \right), \quad (54)$$

where $\kappa = 1$ if \mathcal{C} is convex, $\kappa = 2$ if \mathcal{C} is nonconvex, and:

$$\alpha := \kappa \sqrt{\left(1 - \frac{\lambda}{L}\right) \left(1 - \frac{\lambda + \mu_{\mathcal{C}}}{L}\right)}, \quad (55)$$

$$\delta_k := \mathbb{E} \sup_{\mathbf{v} \in \mathcal{C} \cap \mathcal{B}^n} \mathbf{v}^T \left(\mathcal{F}_{\theta_k}(\mathbf{y}) - \mathbf{u}^\dagger \right), \quad (56)$$

$$\epsilon := \mathbb{E} \sup_{\mathbf{v} \in \mathcal{C} \cap \mathcal{B}^n} \mathbf{v}^T \mathbf{A}^T \mathbf{w}. \quad (57)$$

Proof Recall the iteration of PnP-FEI in the form of:

$$\mathbf{u}_{k+1} = \mathcal{D}(\mathbf{u}_k - \eta[\nabla f_{\text{mc}}(\mathbf{y}, \mathbf{A}\mathbf{u}_k) + \lambda(\mathbf{u}_k - \mathcal{F}_{\theta_k}(\mathbf{y}))]), \quad (58)$$

we can bound the iterative output $\|\mathbf{u}_{k+1} - \mathbf{u}^\dagger\|_2$ with assumptions and several manipulations:

$$\begin{aligned} \|\mathbf{u}_{k+1} - \mathbf{u}^\dagger\|_2 &= \|\mathcal{D}(\mathbf{u}_k - \eta(\mathbf{A}^T(\mathbf{A}\mathbf{u}_k - \mathbf{y}) + \lambda(\mathbf{u}_k - \mathcal{F}_{\theta_k}(\mathbf{y})))) - \mathbf{u}^\dagger\|_2 \\ &\leq \|P_{\mathcal{M}}(\mathbf{u}_k - \eta(\mathbf{A}^T(\mathbf{A}\mathbf{u}_k - \mathbf{y}) + \lambda(\mathbf{u}_k - \mathcal{F}_{\theta_k}(\mathbf{y})))) - \mathbf{u}^\dagger\|_2 \\ &\quad + \|e(\mathbf{u}_k - \eta(\mathbf{A}^T(\mathbf{A}\mathbf{u}_k - \mathbf{y}) + \lambda(\mathbf{u}_k - \mathcal{F}_{\theta_k}(\mathbf{y}))))\|_2 \\ &\leq \|P_{\mathcal{M}}(\mathbf{u}_k - \eta(\mathbf{A}^T(\mathbf{A}\mathbf{u}_k - \mathbf{y}) + \lambda(\mathbf{u}_k - \mathcal{F}_{\theta_k}(\mathbf{y})))) - \mathbf{u}^\dagger\|_2 + \mathcal{E}_0 \\ &\leq \|P_{\mathcal{M}-\mathbf{u}^\dagger}(\mathbf{u}_k - \mathbf{u}^\dagger - \eta(\mathbf{A}^T(\mathbf{A}\mathbf{u}_k - \mathbf{y}) + \lambda(\mathbf{u}_k - \mathcal{F}_{\theta_k}(\mathbf{y}))))\|_2 + \mathcal{E}_0 \\ &\leq \kappa \|P_{\mathcal{C}}(\mathbf{u}_k - \mathbf{u}^\dagger - \eta(\mathbf{A}^T(\mathbf{A}\mathbf{u}_k - \mathbf{y}) + \lambda(\mathbf{u}_k - \mathcal{F}_{\theta_k}(\mathbf{y}))))\|_2 + \mathcal{E}_0 \\ &\leq \kappa \sup_{\mathbf{v} \in \mathcal{C} \cap \mathcal{B}^n} \mathbf{v}^T (\mathbf{u}_k - \mathbf{u}^\dagger - \eta(\mathbf{A}^T(\mathbf{A}\mathbf{u}_k - \mathbf{A}\mathbf{u}^\dagger - \mathbf{w}) + \lambda(\mathbf{u}_k - \mathcal{F}_{\theta_k}(\mathbf{y})))) + \mathcal{E}_0 \\ &\leq \kappa \sup_{\mathbf{v} \in \mathcal{C} \cap \mathcal{B}^n} \mathbf{v}^T \left(\left((1 - \eta\lambda)\mathbf{I} - \eta\mathbf{A}^T\mathbf{A} \right) (\mathbf{u}_k - \mathbf{u}^\dagger) + \eta\lambda (\mathcal{F}_{\theta_k}(\mathbf{y}) - \mathbf{u}^\dagger) + \eta\mathbf{A}^T\mathbf{w} \right) + \mathcal{E}_0 \\ &\leq \kappa \left\| \left((1 - \eta\lambda)\mathbf{I} - \eta\mathbf{A}^T\mathbf{A} \right) (\mathbf{u}_k - \mathbf{u}^\dagger) \right\|_2 + \kappa\eta\lambda \sup_{\mathbf{v} \in \mathcal{C} \cap \mathcal{B}^n} \mathbf{v}^T (\mathcal{F}_{\theta_k}(\mathbf{y}) - \mathbf{u}^\dagger) \\ &\quad + \kappa\eta \sup_{\mathbf{v} \in \mathcal{C} \cap \mathcal{B}^n} \mathbf{v}^T \mathbf{A}^T \mathbf{w} + \mathcal{E}_0 \end{aligned}$$

then taking expectation, we have

$$\mathbb{E}\|\mathbf{u}_{k+1} - \mathbf{u}^\dagger\|_2 \leq \kappa\mathbb{E}\left\| \left((1 - \eta\lambda)\mathbf{I} - \eta\mathbf{A}^T\mathbf{A} \right) (\mathbf{u}_k - \mathbf{u}^\dagger) \right\|_2 + \kappa\eta(\lambda\delta_k + \epsilon) + \mathcal{E}_0,$$

with

$$\begin{cases} \delta_k := \mathbb{E} \sup_{\mathbf{v} \in \mathcal{C} \cap \mathcal{B}^n} \mathbf{v}^T (\mathcal{F}_{\theta_k}(\mathbf{y}) - \mathbf{u}^\dagger); \\ \epsilon := \mathbb{E} \sup_{\mathbf{v} \in \mathcal{C} \cap \mathcal{B}^n} \mathbf{v}^T \mathbf{A}^T \mathbf{w}, \end{cases}$$

then apply Jensen's inequality:

$$\begin{aligned} \mathbb{E} \|\mathbf{u}_{k+1} - \mathbf{u}^\dagger\|_2 &\leq \kappa \sqrt{\mathbb{E} \|((1 - \eta\lambda)\mathbf{I} - \eta\mathbf{A}^T \mathbf{A})(\mathbf{u}_k - \mathbf{u}^\dagger)\|_2^2} + \kappa\eta(\lambda\delta_k + \epsilon) + \mathcal{E}_0 \\ &\leq \kappa \mathbb{E} \{ \|(1 - \eta\lambda)(\mathbf{u}_k - \mathbf{u}^\dagger)\|_2^2 - 2\eta(1 - \eta\lambda) \|\mathbf{A}(\mathbf{u}_k - \mathbf{u}^\dagger)\|_2^2 + \eta^2 L \|\mathbf{A}(\mathbf{u}_k - \mathbf{u}^\dagger)\|_2^2 \}^{1/2} \\ &\quad + \kappa\eta(\lambda\delta_k + \epsilon) + \mathcal{E}_0 \\ &\leq \kappa \mathbb{E} \{ ((1 - \eta\lambda)^2 - \eta(2 - \eta\lambda - \eta L)\mu_C) \|\mathbf{u}_k - \mathbf{u}^\dagger\|_2^2 \}^{1/2} + \kappa\eta(\lambda\delta_k + \epsilon) + \mathcal{E}_0 \end{aligned}$$

then set $\eta = \frac{1}{L}$, we have

$$\begin{aligned} \mathbb{E} \|\mathbf{u}_{k+1} - \mathbf{u}^\dagger\|_2 &\leq \kappa \mathbb{E} \left\{ \left[\left(1 - \frac{\lambda}{L}\right)^2 - \frac{1}{L} \left(1 - \frac{\lambda}{L}\right) \mu_C \right] \|\mathbf{u}_k - \mathbf{u}^\dagger\|_2^2 \right\}^{1/2} + \frac{\kappa}{L} (\lambda\delta_k + \epsilon) + \mathcal{E}_0 \\ &\leq \kappa \sqrt{\left(1 - \frac{\lambda}{L}\right) \left(1 - \frac{\lambda + \mu_C}{L}\right)} \|\mathbf{u}_k - \mathbf{u}^\dagger\|_2 + \frac{\kappa}{L} (\lambda\delta_k + \epsilon) + \mathcal{E}_0 \end{aligned}$$

let $\alpha := \kappa \sqrt{\left(1 - \frac{\lambda}{L}\right) \left(1 - \frac{\lambda + \mu_C}{L}\right)}$, we can tower up to:

$$\mathbb{E} \|\mathbf{u}_{K+1} - \mathbf{u}^\dagger\|_2 \leq \alpha^K \|\mathbf{u}_0 - \mathbf{u}^\dagger\|_2 + \frac{1 - \alpha^K}{1 - \alpha} \left(\kappa \frac{(\sum_{j=1}^K \lambda\delta_k + \epsilon)}{L} + \mathcal{E}_0 \right),$$

this finish the proof. ■

References

- Manya V Afonso, José M Bioucas-Dias, and Mário AT Figueiredo. Fast image recovery using variable splitting and constrained optimization. *IEEE transactions on image processing*, 19(9):2345–2356, 2010.
- Chinmay Belthangady and Loic A Royer. Applications, promises, and pitfalls of deep learning for fluorescence image reconstruction. *Nature methods*, 16(12):1215–1225, 2019.
- Anadi Chaman and Ivan Dokmanić. Truly shift-equivariant convolutional neural networks with adaptive polyphase upsampling. In *2021 55th Asilomar Conference on Signals, Systems, and Computers*, pages 1113–1120. IEEE, 2021.
- Stanley H Chan, Xiran Wang, and Omar A Elgendy. Plug-and-play admm for image restoration: Fixed-point convergence and applications. *IEEE Transactions on Computational Imaging*, 3(1):84–98, 2016.
- Dongdong Chen, Julián Tachella, and Mike E Davies. Equivariant imaging: Learning beyond the range space. In *Proceedings of the IEEE/CVF International Conference on Computer Vision*, pages 4379–4388, 2021.

- Dongdong Chen, Julián Tachella, and Mike E Davies. Robust equivariant imaging: a fully unsupervised framework for learning to image from noisy and partial measurements. In Proceedings of the IEEE/CVF Conference on Computer Vision and Pattern Recognition, pages 5647–5656, 2022.
- Zhixiang Chi, Yang Wang, Yuanhao Yu, and Jin Tang. Test-time fast adaptation for dynamic scene deblurring via meta-auxiliary learning. In Proceedings of the IEEE/CVF conference on computer vision and pattern recognition, pages 9137–9146, 2021.
- Kenneth Clark, Bruce Vendt, Kirk Smith, John Freymann, Justin Kirby, Paul Koppel, Stephen Moore, Stanley Phillips, David Maffitt, Michael Pringle, et al. The cancer imaging archive (tcia): maintaining and operating a public information repository. Journal of digital imaging, 26:1045–1057, 2013.
- K Dabov, A Foi, V Katkovnik, and K Egiazarian. Image denoising by sparse 3-d transform-domain collaborative filtering. IEEE transactions on image processing: a publication of the IEEE Signal Processing Society, 16(8):2080–2095, 2007.
- Mohammad Zalbagi Darestani, Jiayu Liu, and Reinhard Heckel. Test-time training can close the natural distribution shift performance gap in deep learning based compressed sensing. In International conference on machine learning, pages 4754–4776. PMLR, 2022.
- Olivier Devolder, François Glineur, and Yurii Nesterov. First-order methods of smooth convex optimization with inexact oracle. Mathematical Programming, 146(1):37–75, 2014.
- Chao Dong, Chen Change Loy, Kaiming He, and Xiaoou Tang. Image super-resolution using deep convolutional networks. IEEE transactions on pattern analysis and machine intelligence, 38(2):295–307, 2015.
- Matthias Joachim Ehrhardt, Zeljko Kereta, Jingwei Liang, and Junqi Tang. A guide to stochastic optimisation for large-scale inverse problems. Inverse Problems, 2025.
- Jia-Bin Huang, Abhishek Singh, and Narendra Ahuja. Single image super-resolution from transformed self-exemplars. In Proceedings of the IEEE conference on computer vision and pattern recognition, pages 5197–5206, 2015.
- Peizhou Huang, Chaoyi Zhang, Xiaoliang Zhang, Xiaojuan Li, Liang Dong, and Leslie Ying. Self-supervised deep unrolled reconstruction using regularization by denoising. IEEE transactions on medical imaging, 43(3):1203–1213, 2023.
- Gary Mataev, Peyman Milanfar, and Michael Elad. Deepred: Deep image prior powered by red. In Proceedings of the IEEE/CVF International Conference on Computer Vision Workshops, pages 0–0, 2019.
- Vishal Monga, Yuelong Li, and Yonina C Eldar. Algorithm unrolling: Interpretable, efficient deep learning for signal and image processing. IEEE Signal Processing Magazine, 38(2):18–44, 2021.
- Y. Nesterov. Gradient methods for minimizing composite objective function. Technical report, UCL, 2007.
- Yurii Nesterov. A method of solving a convex programming problem with convergence rate $o(1/k^2)$. In Soviet Mathematics Doklady, volume 27, pages 372–376, 1983.

- Samet Oymak, Benjamin Recht, and Mahdi Soltanolkotabi. Sharp time–data tradeoffs for linear inverse problems. *IEEE Transactions on Information Theory*, 64(6):4129–4158, 2017.
- Seobin Park, Jinsu Yoo, Donghyeon Cho, Jiwon Kim, and Tae Hyun Kim. Fast adaptation to super-resolution networks via meta-learning. In *European conference on computer vision*, pages 754–769. Springer, 2020.
- Xinran Qin, Yuhui Quan, Tongyao Pang, and Hui Ji. Ground-truth free meta-learning for deep compressive sampling. In *Proceedings of the IEEE/CVF Conference on Computer Vision and Pattern Recognition*, pages 9947–9956, 2023.
- Yuhui Quan, Xinran Qin, Tongyao Pang, and Hui Ji. Dual-domain self-supervised learning and model adaption for deep compressive imaging. In *European Conference on Computer Vision*, pages 409–426. Springer, 2022.
- Marc Robini, Yuemin Zhu, Xudong Lv, and Wanyu Liu. Inexact half-quadratic optimization for image reconstruction. In *2016 IEEE International Conference on Image Processing (ICIP)*, pages 3513–3517. IEEE, 2016.
- Marc C Robini, Feng Yang, and Yuemin Zhu. Inexact half-quadratic optimization for linear inverse problems. *SIAM Journal on Imaging Sciences*, 11(2):1078–1133, 2018.
- Olaf Ronneberger, Philipp Fischer, and Thomas Brox. U-net: Convolutional networks for biomedical image segmentation. In Nassir Navab, Joachim Hornegger, William M. Wells, and Alejandro F. Frangi, editors, *Medical Image Computing and Computer-Assisted Intervention – MICCAI 2015*, pages 234–241, Cham, 2015. Springer International Publishing. ISBN 978-3-319-24574-4.
- Emil Y Sidky, Chien-Min Kao, and Xiaochuan Pan. Accurate image reconstruction from few-views and limited-angle data in divergent-beam ct. *Journal of X-ray Science and Technology*, 14(2):119–139, 2006.
- Zhaodong Sun, Fabian Latorre, Thomas Sanchez, and Volkan Cevher. A plug-and-play deep image prior. In *ICASSP 2021-2021 IEEE International Conference on Acoustics, Speech and Signal Processing (ICASSP)*, pages 8103–8107. IEEE, 2021.
- Julián Tachella, Dongdong Chen, and Mike Davies. Unsupervised learning from incomplete measurements for inverse problems. *Advances in Neural Information Processing Systems*, 35:4983–4995, 2022.
- Julián Tachella, Mike Davies, and Laurent Jacques. Unsure: Unknown noise level stein’s unbiased risk estimator. *arXiv preprint arXiv:2409.01985*, 2024.
- Hong Ye Tan, Subhadip Mukherjee, Junqi Tang, and Carola-Bibiane Schönlieb. Provably convergent plug-and-play quasi-newton methods. *SIAM Journal on Imaging Sciences*, 17(2):785–819, 2024.
- Matthieu Terris, Thomas Moreau, Nelly Pustelnik, and Julian Tachella. Equivariant plug-and-play image reconstruction. In *Proceedings of the IEEE/CVF Conference on Computer Vision and Pattern Recognition*, pages 25255–25264, 2024.
- Dmitry Ulyanov, Andrea Vedaldi, and Victor Lempitsky. Deep image prior. In *Proceedings of the IEEE Conference on Computer Vision and Pattern Recognition*, pages 9446–9454, 2018.

- Singanallur V Venkatakrishnan, Charles A Bouman, and Brendt Wohlberg. Plug-and-play priors for model based reconstruction. In 2013 IEEE Global Conference on Signal and Information Processing, pages 945–948. IEEE, 2013.
- Andrew Wang and Mike Davies. Perspective-equivariant imaging: an unsupervised framework for multi-spectral pansharpening. arXiv preprint arXiv:2403.09327, 2024.
- Zhiwen Wang, Zexin Lu, Tao Wang, Ziyuan Yang, Hui Yu, Zhongxian Wang, Yinyu Chen, Jingfeng Lu, and Yi Zhang. Test-time adaptation via orthogonal meta-learning for medical imaging. IEEE Transactions on Radiation and Plasma Medical Sciences, 2024.
- Bo Xin, Yizhou Wang, Wen Gao, David Wipf, and Baoyuan Wang. Maximal sparsity with deep networks? Advances in Neural Information Processing Systems, 29, 2016.
- Guixian Xu, Jinglai Li, and Junqi Tang. Sketched equivariant imaging regularization and deep internal learning for inverse problems. arXiv preprint arXiv:2411.05771, 2024.
- Junfeng Yang and Xiaoming Yuan. Linearized augmented lagrangian and alternating direction methods for nuclear norm minimization. Mathematics of computation, 82(281):301–329, 2013.
- Yan Yang, Jian Sun, Huibin Li, and Zongben Xu. Admm-csnet: A deep learning approach for image compressive sensing. IEEE transactions on pattern analysis and machine intelligence, 42(3):521–538, 2018.
- Jiahui Yu, Zhe Lin, Jimei Yang, Xiaohui Shen, Xin Lu, and Thomas S Huang. Free-form image inpainting with gated convolution. In Proceedings of the IEEE/CVF international conference on computer vision, pages 4471–4480, 2019.
- Jure Zbontar, Florian Knoll, Anuroop Sriram, Tullie Murrell, Zhengnan Huang, Matthew J. Muckley, Aaron Defazio, Ruben Stern, Patricia Johnson, Mary Bruno, Marc Parente, Krzysztof J. Geras, Joe Katsnelson, Hersh Chandarana, Zizhao Zhang, Michal Drozdal, Adriana Romero, Michael Rabbat, Pascal Vincent, Nafissa Yakubova, James Pinkerton, Duo Wang, Erich Owens, C. Lawrence Zitnick, Michael P. Recht, Daniel K. Sodickson, and Yvonne W. Lui. fastmri: An open dataset and benchmarks for accelerated mri, 2019. URL <https://arxiv.org/abs/1811.08839>.
- Jian Zhang and Bernard Ghanem. Ista-net: Interpretable optimization-inspired deep network for image compressive sensing. In Proceedings of the IEEE conference on computer vision and pattern recognition, pages 1828–1837, 2018.
- Kai Zhang, Wangmeng Zuo, Yunjin Chen, Deyu Meng, and Lei Zhang. Beyond a gaussian denoiser: Residual learning of deep cnn for image denoising. IEEE Transactions on Image Processing, 26(7):3142–3155, 2017.
- Kai Zhang, Luc Van Gool, and Radu Timofte. Deep unfolding network for image super-resolution. In Proceedings of the IEEE/CVF conference on computer vision and pattern recognition, pages 3217–3226, 2020.
- Yutian Zhao, Tianjing Zhang, and Hui Ji. Test-time model adaptation for image reconstruction using self-supervised adaptive layers. In European Conference on Computer Vision, pages 111–128. Springer, 2024.

Qingping Zhou, Jiayu Qian, Junqi Tang, and Jinglai Li. Deep unrolling networks with recurrent momentum acceleration for nonlinear inverse problems. Inverse Problems, 40(5):055014, 2024.